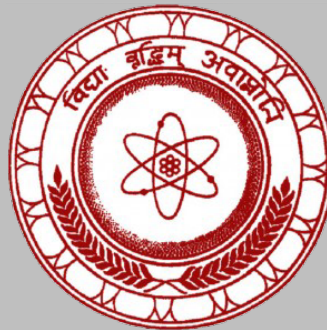


ISSN 1391-0256

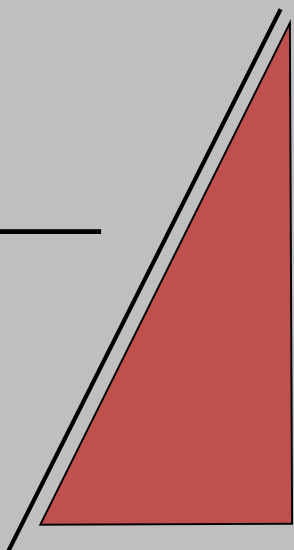
Journal of the Sri Lanka Association for the Advancement of Science

Volume 6 Issue 1, 2024



JSLAAS

Founded in 1944 and incorporated by the Act of Parliament No 11 of 1966.



Journal of the Sri Lanka Association for the Advancement of Science is a biannual publication. Selected research work from annual research sessions (based on scientific merit) as well as other research articles are invited to submit research manuscripts as per the guidelines provided by SLAAS. SLAAS members may also separately submit their papers for publication. The Journal can be accessed on-line to view and download the full text of the articles published respective to the volumes free of charge

Submission Manuscript

Only online submission, Web: <https://journal.slaas.lk>, e-ISSN: 2682-6992

Members of the Editorial Board

Editor in Chief

Prof. K P S Chandana Jayaratne
Department of Physics
University of Colombo,
Sri Lanka.
email: chandana Jayaratne@gmail.com

Co- Editor

Dr. R Chinthaka L De Silva
Materials Technology Section
Industrial Technology Institute
Sri Lanka.
363, Baudhaloka Mw, Colombo, Sri Lanka.
email: chinthakades@yahoo.com

General President SLAAS 2024

Prof. Ramani D. Wijesekera
Dept. of Chemistry
University of Colombo
Colombo 03
email: ramanee@chem.cmb.ac.lk

International Editorial Advisory Board

Prof. Don Nalin Nilusha Wijayawardene
Dr. Udara Abeyssekera
Prof. Hemamala Karunadasa
Dr. M Wasim Siddiqui

Managing Editor

Dr. Lochandaka Ranathunga
Department of Information Technology
Faculty of Information Technology
University of Moratuwa, Sri Lanka
email: lochandaka@uom.lk

Editorial Board

Prof. Mahesh Jayaweera
Prof. B C Liyanage Athapattu
Prof. Chandana Abeysinghe
Prof. G M K B Gunaherath
Prof. S Vasanthapriyan
Prof. Prasanthi Gunawardene
Dr. K M G P Yahampath
Dr. Thanuja Paragoda
Dr. Jasotha Prabagar

Sectional Representatives

Dr. K R M Chandrathilaka
Ms. J K P C Jayawardhana
Mr. H Siriwardana
Dr. Uthpala Jayawardena
Dr. S A K P De Silva
Dr. Induni W Siriwardane
Dr. K A K T Karunanayaka
Ms. Nethini Ganepola

Exchanges: Please address all requests to the Secretary, Sri Lanka Association for the Advancement of Science, "Vidya Mandiraya" 120/10, Wijerama Mawatha Colombo 07, Sri Lanka

Table of Contents

	Page
1 Effect of CT Simulator Tube Voltages on CT Number and Relative Electron Density of CT Images <i>D P De Sliva, A H Dilip Kumara, K L Priyalal, K L I Gunawardhana</i>	04
2 Incorporation of Wood ash and waste glass powder in enhancing concrete block performance <i>P V T Prarthana, R C L De Silva, P Subramanium, S Thuraisingam, J Prabagar</i>	17
3 Low-Pressure and Atmospheric-Pressure Cold Plasma Treatment as a Pretreatment for Extracting Volatile Oils from Black Pepper (<i>Piper nigrum</i>) Seeds <i>A B G C J De Silva, H D Weerathunge, P N R J Amunugoda, S H P Gunawrdena, A A P de Alwis</i>	25
4 Photocatalytic degradation of methylene blue dye using silver nanoparticles prepared from <i>Raphanus sativus</i> <i>M Y F Hasna, S Anuluxan, S Prabagar, R C L De Silva, S Thuraisingam, J Prabagar</i>	39

Effect of CT Simulator Tube Voltages on CT Number and Relative Electron Density of CT Images

D P De Sliva^{1*}, A H Dilip Kumara¹, K L Priyalal¹, K L I Gunawardhana¹

¹ Department of Radiotherapy, Cancer Unit, Teaching Hospital Karapitiya, Sri Lanka

ABSTRACT

The radiotherapy treatment planning for the cancer patient begins with the imaging of the patient using a Computed Tomography (CT) simulator. The CT simulator determines the locations and densities of patient organs using pixels. Each pixel has a unit called a CT number, or Hounsfield Unit (HU), to express the quantity of radiation attenuation in patient tissues. The density of human tissue is presented in Relative Electron Density (RED). The conversion relationship between RED and CT numbers is required to be determined and fed to the Treatment Planning System (TPS). The TPS calculates the radiotherapy dose for the patient using this CT-RED conversion curve. Most TPSs contain a single CT-RED curve defined at a specific CT tube voltage.

In this research, we studied the effect of CT tube voltages using a CT simulator (GE; CT-RED curve defined at 140kV) at Teaching Hospital Karapitiya, which provides step voltages of 80 kV, 120 kV, and 140 kV, XIO TPS, and Thorax Phantom (CIRS) containing 5 tissue types. According to the measured results, CT numbers decrease with increasing CT Tube voltage. Also, there were no significant errors in RED values of tissues at 120 kV, with respect to the 140 kV. But there were 5.55%, 2.10%, 0.99%, 0.99%, 0.95%, and 1.34% errors in RED for lung, adipose, water, T1420, muscle, and bone tissues respectively at 80kV with respect to 140 kV.

Key Words: Radiotherapy, CT imaging, CT Number, CT tube voltage, Relative Electron Density

INTRODUCTION

The determination of dose distribution within the treated volume is an essential step of modern treatment planning in radiotherapy. Many factors influence the dose distribution, and the heterogeneity of the patient's body is one of them (Parker et al., 1979). Data customization for each patient is therefore required for the dose calculations. Computed Tomography (CT) has been used as a fundamental source of such data for over 30 years now and is used as a foundation for treatment planning. Furthermore, the presentation of CT is fundamental, as it provides information on the attenuation of radiation by the patient's tissues in the form of CT numbers, expressed in Hounsfield Units (HUs) as in the following equation (Bryant et al., 2012):

$$HU_{\text{tissue}} = [(\mu_{\text{tissue}} - \mu_{\text{water}}) / \mu_{\text{water}}] \times 1,000 \quad (1)$$

Where μ_{tissue} is the linear attenuation coefficient of tissue and μ_{water} is the linear attenuation coefficient of water. It is known that a precise calculation of dose distribution in radiotherapy can be performed based on the fundamental knowledge of the Relative Electron Density (RED) of the tissues. Treatment Planning Systems (TPS) usually convert HU values to RED (normalized to water) using the predefined relationship (CT to RED curve) between the two quantities (Witold et al., 2010). In some TPS, the relationship is fixed (CT-RED curve is fixed at the XiO TPS used for treatment planning of cobalt machine of Teaching Hospital Karapitiya); in others, the user can change it.

HUs for a given tissue depend on the quality of the X-ray beam; therefore, the values can differ between scanners. Even for a single scanner, CT numbers for the same tissue depend on the tube voltage. Different tube voltages are selected for CT scan imaging to obtain a quality image. As an example, if CT scans are obtained using 80 kV instead of 140 kV while using the same CT-RED relationship obtained at 140 kV, the dose calculated by TPS can be inaccurate. The CT-RED relationships can be measured during the calibration of a CT simulator with the use of body phantoms containing tissue-equivalent materials, i.e., materials that have an atomic composition similar to human tissues. The accuracy of dose distribution depends on the accuracy of the CT number and RED values that are defined by the TPS (Witold et al., 2010).

The main objective of this research work is to study the effect of CT simulator tube voltages on CT number and RED of images. Here, we have a single CT to RED curve. Since the accuracy of RED directly affects calculations of radiotherapy dose distribution the findings of this research work will be very important. Also, measuring the linear attenuation coefficient and calculating the average CT number of tissue equivalent materials for three different tube voltages are the specific objectives of this work.

INSTRUMENTATION, THEORY&METHODOLOGY



Figure 1: The GE CT Simulator (Source:<https://ctmedicalscanners.com/ge-lightspeed-rt-16-ct-scanner/>)

A CT (Computed-Tomography) Simulator consists of a CT scanner with a flat tabletop, a patient positioning and marking system with external lasers, CT-simulation 3D treatment planning software, and various hardcopy output devices. The CT scanner is used to acquire a volumetric CT scan of a patient, which represents the “virtual” or digital patient. The CT simulation software provides virtual representations of the geometric capabilities of a treatment machine (Sherouse and Chaney, 2003). This software can be a special virtual simulation program or it can be a component of a treatment planning system. Often, CT simulation is referred to as virtual simulation and the two terms tend to be used interchangeably. Virtual simulation is used to define any simulation based on software created “virtual simulator” and a volumetric patient scan. The following Table 1 shows the different tissue types with their density values and HU values using the Advanced Signal Processing Handbook (Stergios, 2003).

Table 1: CT numbers of Tissue Types (Stergios, 2003)

Tissue type	Density (g/cm ³)	HU
Air	0.001	-1000.0±05.0
Lung	0.300	-706.3±23.3
Adipose	0.920	-86.8±18.1
Breast	0.990	-20.3±15.1
Muscle	1.060	-21.0±10.0
Water	1.015	0±00.5
Brain	1.045	30.9±15.2
Liver	1.080	94.5±17.2
Inner bone	1.120	60.3±17.9
Bone Mineral	1.145	238.0±19.6
Cortical Bone	1.840	1273.1±19.8

The gamma-ray linear attenuation coefficient describes the absorption of gamma rays per unit length of an absorber material. This quantity depends on the energy of the incident gamma-ray beam and the density of the absorptive material. It is expressed numerically in units of m^{-1} (Ermis and Celiktas, 2012).

When a pencil gamma beam with the intensity of I_0 transmits perpendicularly with an absorber of thickness x , the intensity (I) passing through the absorber can be evaluated by equation 2

$$I = I_0 e^{-\mu x} \quad (2)$$

CT measures the attenuation coefficient of an object and converts the value assigned to each voxel into a CT number, and the absorbed dose to a patient in radiation therapy is calculated using the RED of each voxel in the CT image of the patient. The correlation between the CT number and the electron density is derived from a CT scan of the materials with known RED and the points between the derived relations are filled up by interpolations. This relation is applied during the dose calculation based on the CT image and thus, the accurate measurement of CT number and applying the value to the treatment planning system (TPS) is fundamental to radiation therapy. The attenuation coefficient varies with a chosen X-ray tube voltage (kV) from the CT scanner since the attenuation coefficient has an energy-dependent property and has discovered significant CT number changes in different kV for most materials.

The maximum difference between the real values of RED (as given by the manufacturers of the phantom) and the RED obtained by the TPS should not exceed 0.05 (Tolerance level) (Seco and Evans, 2006).

The CT simulator machine and CMS XiO TPS of Teaching Hospital Karapitiya were used to carry out this research project. All the experiments were conducted at the radiotherapy unit of Teaching Hospital Karapitiya. The CT simulator machine at Teaching Hospital Karapitiya contains a voltage generator that can be operated for 80 kV, 120 kV, 140 kV, and 10 mA to 440 mA in 5 mA increments.

CIRS (brand name) Thorax Phantom (model 002LFC) and five tissue equivalent rods were used in this experiment. Tissue-equivalent rods are removable, and they can be inserted into the holes in the CIRS phantom. Electron density relative to water is known, and a distilled water syringe was used for experiments.



Figure 2: CIRS Body Phantom

The PTW 30010 chamber and UNIDOS electrometer were selected as suitable measuring devices for the experiments. PTW 30010 chamber (sensitive volume: 0.6 cm³) responses for energy range: 30 keV–50 keV photon and electron radiation. The UNIDOS electrometer contains an accuracy of $\pm 0.5\% \pm 1$ digit.



Figure 3: Experimental Setup

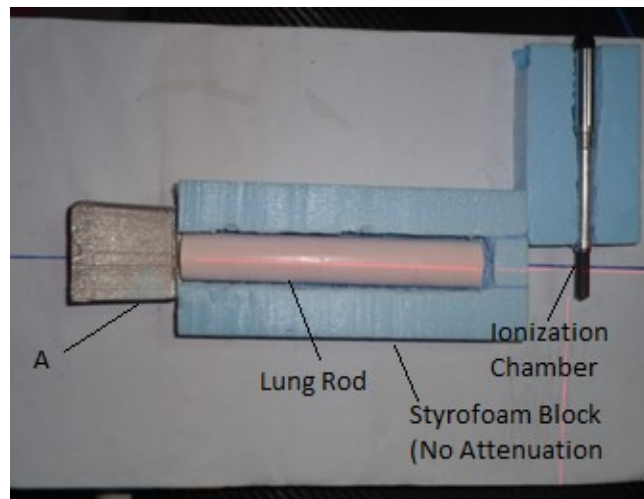


Figure 4: Experimental Setup (Lung Rod)

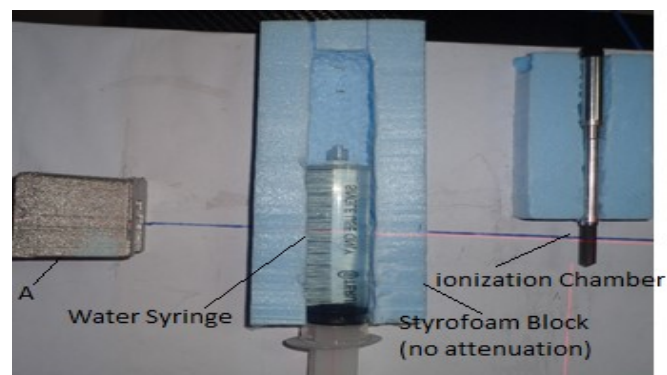


Figure 5: Experimental Setup (Water Syringe)

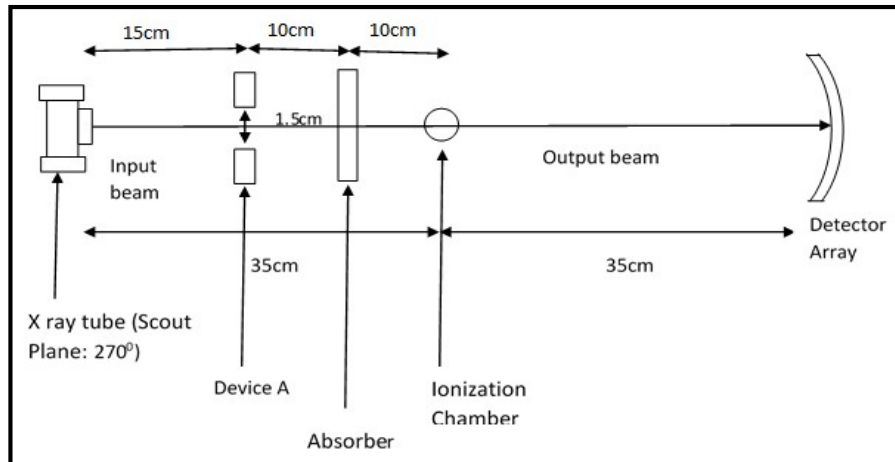


Figure 6: Experimental Setup

The experimental setup was arranged on the couch of the CT machine as above. The distance between the absorbance material and the ionization chamber, as well as the distance between the absorbance material and the X-ray head, was maintained as same. The attenuation factor of the air gap affects the measurements. The lead attenuator marked A was designed and made by using lead alloy in the mould room of Teaching Hospital Karapitiya. The purpose of the attenuator is to cut off the diverged X-ray beams and measure the narrowed X-ray beam that is perpendicular to the absorber. The isocenter of the setup (focus) was selected at the effective point (center) of the ionization chamber (Figure 3).

The study was carried out at three CT tube voltages: 80 kV, 120 kV, and 140 kV, respectively, at a constant tube current (80 mA). Five lateral X-rays (Scout plane: 270°) were measured without an absorber for each energy level to obtain a significant reading on the electrometer. This reading was considered the incident X-ray beam intensity (Figure 3). There is no tube rotation during the scout scan process. The field length of CT scanning is defined by the longitudinal distance of couch movement.

During this research project, couch movement distance was maintained as a constant for a scout image (5 cm of couch movement within 1.9 s duration). That causes the ion chamber reading to maintain the same scatter effect during the couch (experimental setup) movement that is required to complete the scout scan process. The window of the X-ray beam attenuator (device A) is 1.5 cm x 2.0 cm, and the CT simulator produces the fan beam geometry X-ray beam output of 1mm (scan mode: 2 slices x 0.5 mm). Therefore, the cross-sectional dimension of the input X-ray beam incident on the absorber is 0.36 mm x 2.5 cm. The cross-sectional dimension of the output X-ray beam incident on the ionization chamber is 0.50 mm x 3.0 cm. The dimensions were calculated according to the divergence of the X-ray beam. Then absorbance material was kept between device A and the ionization chamber, and the output was measured by applying five lateral X-rays (Scout plane 270°) for the above three CT tube voltage sat 80 mA (Figure 4, and Figure 5). The same couch movement distance (5 cm) and time duration (1.9 s) were maintained for all measurements.

The average absorber thickness has been changed in an appropriate way to obtain a significant electrometer reading. As an example, if a photon beam was transmitted through the 16-cm length of the bone rod, the meter reading was not sufficient to obtain due to higher attenuation. Also, at lower kV (80 kV), the meter

reading was not detected even with a 5 cm absorber thickness. Correction was done to omit the attenuation of the syringe wall during the experiments conducted with water.

RESULTS AND DISCUSSION

The above setup (Figure 6) has been used to carry out the experiments, as a narrowed photon beam has been used for the experiments and the ionization chamber diameter is very low (0.61 cm) compared to the rod diameter (2.5cm). Linear attenuation coefficients of selected absorbance materials were calculated by using Equation 2. When a pencil gamma beam with an intensity of I_0 transmits perpendicularly with an absorber of thickness x , the intensity (I) passing through the absorber can be evaluated by equation 2, μ is the x-ray attenuation coefficient of the absorbent material. Then CT numbers of different absorbance materials were calculated in HU units by using equation 1 for different kV settings.

Measuring the CT number and RED of selected materials using the TPS was done by conducting experiments with the XiO TPS. All the absorbance materials were set up on the couch of the CT simulator machine, obtained CT images at corresponding energy levels, and transferred to the TPS. (Slice Thickness: 0.5 cm, Tube Current: 80 mA). During the image loading, the CT number to relative electron density conversion process has been selected. This process is performed by the radiotherapy TPS by using the predefined CT number to RED conversion curve (Figure 7) defined at 140 kV. That curve is the only curve available in this XiOTPS.

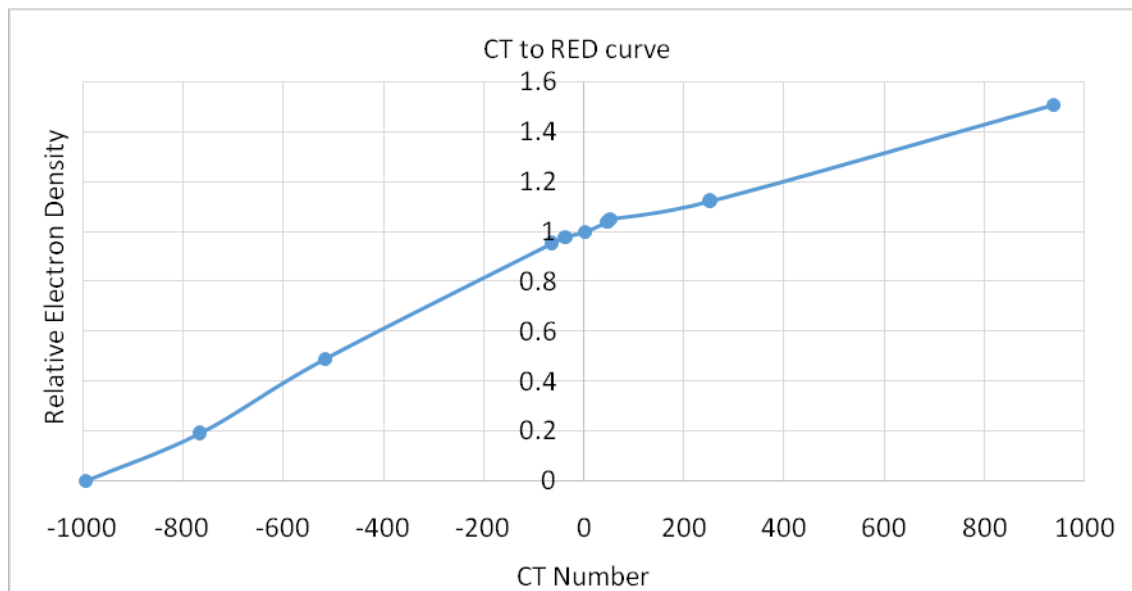


Figure 7: CT-RED curve derived in TPS defined at 140 kV

All the images were prepared as required for the planning process (similar to body outlining). The maximum value, minimum value, and mean value of CT numbers were obtained by selecting an ROI (Region of Interest). RED values were observed with the same window by following the same procedures as above.

Experimentally calculated linear attenuation coefficients and CT number values are presented in Table 2 at 80 kV, 120 kV, and 140 kV.

Table 2: Experimentally calculated linear attenuation values and CT values

Absorber Material	Density kgm^{-3}	80 kV setting		120 kV setting		140 kV setting	
		$\mu(\text{m}^{-1})$	CT valve	$\mu(\text{m}^{-1})$	CT valve	$\mu(\text{m}^{-1})$	CT valve
Water	1000	20.50	0	17.68	0	17.53	0
Lung	210	10.43	-491	4.33	-755	3.69	-789
Adipose	960	18.23	-124	16.58	-62	15.82	-97
Soft Tissue T1420	1030	21.19	33	18.17	27	17.66	7
Muscle	1060	24.39	189	18.78	62	18.66	64
Bone	1600	45.58	1223	36.18	1046	31.62	803

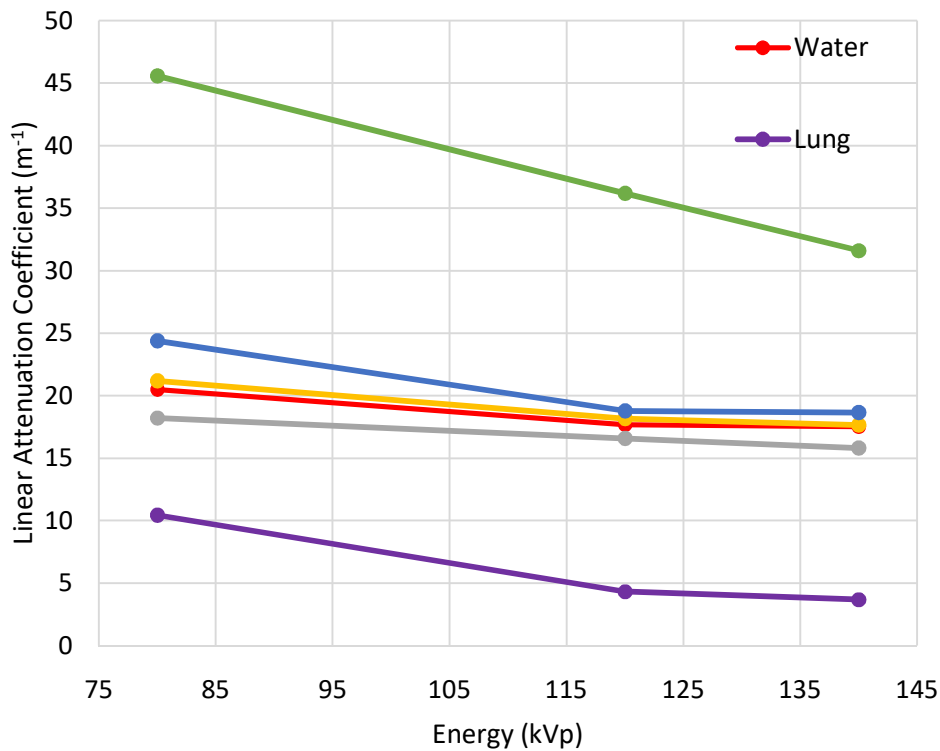


Figure 8: Variation of linear attenuation coefficient values with kV for human tissues

CT number values and RED values obtained through TPS are presented in Table 3 and Table 4.

Table 3: Average CT number values obtained by TPS

Absorber Material	80 kV, 80 mA CT value	120 kV, 80 mA CT value	140 kV, 80 mA CT value
Water	5	3	3
Lung	-620	-780	-783
Adipose	-130	-68	-58
T1420(Soft Tissue)	20	6	11
Muscle	155	140	85
Bone	1235	945	907

Table 4: Average RED values obtained by TPS

Absorber Material	RED (IAEA TECDOC 1583)	140 kV, 80 mA RED	80 kV, 80 mA RED	% error 80kV (With respect to the 140kV)	120 kV, 80 mA RED	% error 120kV (With respect to the 140kV)
Water	-	1.01	1.02	0.99%	1.01	0
Lung	0.207	0.18	0.19	5.55%	0.18	0
Adipose	0.949	0.95	0.93	2.10%	0.95	0
Soft Tissue T1420	-	1.01	1.02	0.99%	1.01	0
Muscle	1.042	1.05	1.06	0.95%	1.05	0
Bone	1.506	1.49	1.51	1.34%	1.49	0

The maximum difference between the real values of RED (as given by the manufacturers of the phantom) and the RED obtained by the TPS should not exceed 0.05 (Tolerance level)(Seco and Evans, 2006). RED values obtained by the TPS of image sets that were scanned at 140kV, 120kV, and 80kV are within the tolerance level when compared with the RED value given by the manufacturer.

DISCUSSION

Computed tomography (CT) measures the attenuation coefficient of an object and converts the value assigned to each voxel into a CT number. In radiation therapy, the CT number, which is directly proportional to the linear attenuation coefficient, is required to be converted to RED for radiation dose calculation for cancer treatment. However, if various tube voltages were applied to take the patient's CT image without applying the specific CT number to the RED conversion curve, the accuracy of the dose calculation would be unassured. In this study, changes in CT numbers for different materials due to changes in tube voltage were analyzed.

The response of normal tissues to radiation is a deterministic effect. Where, the deterministic effects (or tissue reactions) of ionizing radiation are directly related to the absorbed radiation dose, and the severity of the effect increases as the dose increases. There is a threshold (of the order of magnitude of 0.1 Gy or higher) for the deterministic effect. Below the threshold dose, the effect is not present. This radiation response follows a sigmoidal shape. The steep part of the slope indicates the region where a small deviation in dose may cause large tissue toxicity as tumor control curve and normal tissue damage curve are close together.

Radiotherapy is a compromise between a cure and an acceptable risk of complication. Acceptable risk of complications depends on risk level, organ involved, and severity of complications. The level of risk may differ between physicians and patients. Therefore, it is very important to precisely calculate and deliver the radiotherapy doses. The findings of this research work are very important to improve the accuracy of dose calculation.

In this study, three imaging kV levels (80 kV, 120 kV, and 140 kV) were considered at 80 mA for several tissue equivalent rods (bone, lung, muscle, adipose, soft tissue) of Thorax phantom (CIRS). According to the results, the linear attenuation coefficient quadratically decreases with increasing photon energy as the photoelectric effect and Compton scattering effects are dominant at these energy levels. CT number values obtained by both methods were varied with kV. According to the results, CT numbers decrease with increasing kV.

According to the results of this research work, RED values obtained by using the TPS were slightly varied with kV. The maximum differences between the observed RED values and the real values of RED (as given by the manufacturers of the phantom) were within the tolerance level (<0.05).

The CT to RED curve of XiO TSP is defined at 140 kV and therefore CT number to RED conversion has correctly applied for the 140 kV image set. Therefore, the 140 kV level can be considered as a reference to calculate the % error of RED at the other two kV settings. There were no considerable errors in RED values of tissues at 120 kV, with respect to the 140 kV level even though there were differences in CT numbers at those two kV setting image sets. (The difference between 120kV and 140kV tube voltages is not much larger)

But there are 5.55%, 2.10%, 0.99%, 0.99%, 0.95%, and 1.34% errors in RED for lung, adipose, water, T1420 tissue, muscle, and bone tissues respectively at 80kV, with respect to the 140 kV level.

Same as this study according to Rhee et al. (2015) difference in CT number by different kVps (CT tube voltages) was considerable for most materials except for air where the density is very low and therefore noise affects the more considerably. CT x-ray tube voltage variations have considerable effects on the RED-CT number conversion curves. The differences between RED-CT number curves increase with the increase of CT x-ray tube voltage for the equivalent tissues that have densities more than water density, but below water density, the effect is negligible (Afifi et al., 2020). According to Saini et al. (2021), different kVp setting shows variation in the measured HU values. The highest variation was observed in the case of high-density bone material at the lowest kVp tube voltage.

CONCLUSION

CT number values obtained by both methods were varied with CT tube voltage. According to the results, CT numbers decrease with increasing kV. The 140 kV level was considered as a reference to calculate the percentage error of RED at the other two kV settings. There were no errors in RED values of tissues at 120 kV, with respect to the 140 kV level even though there were differences in CT numbers at those two kV image sets. But there are 5.55%, 2.10%, 0.99%, 0.99%, 0.95%, and 1.34% errors in RED for lung, adipose, water, T1420 tissue, muscle, and bone tissues respectively at 80kV, with respect to the 140 kV level. According to the study, the effect is considerable in bone and lung tissues. Therefore dose distribution calculation errors can be dominant in the chest, head and neck, and pelvic regions. It is required to determine the impact of CT tube voltage variation on radiotherapy dose calculation to ensure and enhance the radiotherapy treatment accuracy.

LIMITATIONS

There were only three kV settings available with our CT simulator machine; therefore, the study was limited to three levels. The available CIRS phantom contained just five types of human tissues, and it also didn't contain any metal inserts (high-density metal implants are inserted in patients).

RECOMMENDATIONS

A CT simulator that contains more kV settings (tube voltages) and a CIRS body phantom that has more human tissue types and metal inserts are more deserving in determining the impact of CT tube voltage on the CT-RED curve for further studies. According to this research work, there is an impact on CT number and RED with different tube voltages. Since radiotherapy dose calculation accuracy is very important to cure a tumour, it is required to determine the effect on dose calculation with varying imaging kV settings (CT tube voltage).

ACKNOWLEDGEMENT

Special words of thanks go to the Director of Teaching Hospital Karapitiya for giving me the approval to access the CT simulator and other facilities of Teaching Hospital Karapitiya. Also, I wish to express my gratitude to all officers and workers of the Department of Radiotherapy Teaching Hospital Karapitiya, who helped me in this task in countless ways.

REFERENCES

1. Ahnesjö, A. and Aspradakis, M.M., (1999). Dose calculations for external photon beams in radiotherapy. *Physics in Medicine & Biology*, 44(11), p.R99.
2. Afifi, M.B., Abdelrazek, A., Deiab, N.A., Abd El-Hafez, A.I. and El-Farrash, A.H., (2020). The effects of CT x-ray tube voltage and current variations on the relative electron density (RED) and CT number conversion curves. *Journal of Radiation Research and Applied Sciences*, 13(1), pp.1-11.
3. Brunckhorst, E., Gershkevitch, E., Ibbott, G., Korf, G., Miller, D. and Schmidt, R., (2008). IAEA-TECDOC-1583 Commissioning of radiotherapy treatment planning systems: testing for typical external beam treatment techniques. Vienna: International Atomic Energy Agency.
4. Bryant, J.A., Drage, N.A. and Richmond, S., (2012). CT number definition. *Radiation Physics and Chemistry*, 81(4), pp.358-361.

5. Camoni, L., Santos, A., Attard, M., Mada, M.O., Pietrzak, A.K., Rac, S., Rep, S., Terwinghe, C., Fragoso Costa, P. and Technologist Committee of the European Association of Nuclear Medicine (EANM), (2020). Best practice for the nuclear medicine technologist in CT-based attenuation correction and calcium score for nuclear cardiology. *European Journal of Hybrid Imaging*, 4, pp.1-20.
6. Claude, K.P., Schandorf, C., Amuasi, J.H. and Tagoe, S.N.A., (2013). Fabrication of a tissue characterization phantom from indigenous materials for computed tomography electron density calibration: peer-reviewed original article. *South African Radiographer*, 51(1), pp.9-17.
7. Constantinou, C., Harrington, J.C. and DeWerd, L.A., (1992). An electron density calibration phantom for CT-based treatment planning computers. *Medical physics*, 19(2), pp.325-327.
8. Cozzi, L., Fogliata, A., Buffa, F. and Bieri, S., (1998). Dosimetric impact of computed tomography calibration on a commercial treatment planning system for external radiation therapy. *Radiotherapy and oncology*, 48(3), pp.335-338.
9. Du Plessis, F.C.P., Willemse, C.A., Lötter, M.G. and Goedhals, L., (2001). Comparison of the Batho, ETAR, and Monte Carlo dose calculation methods in CT-based patient models. *Medical Physics*, 28(4), pp.582-589.
10. Ermis, E. and Celiktas, C., (2012). A Different Way to Determine the Gamma-ray Linear Attenuation Coefficients of Materials. *International Journal of Instrumentation Science*, 1(4), pp.41-44.
11. Guan, H., Yin, F.F. and Kim, J.H., (2002). Accuracy of inhomogeneity correction in photon radiotherapy from CT scans with different settings. *Physics in Medicine & Biology*, 47(17), p.N223.
12. Hubbell, J.H., (1996). Tables of x-ray mass attenuation coefficients and mass energy-absorption coefficients. <http://physics.nist.gov/PhysRefData/XrayMassCoef/>.
13. Jones, A.O. and Das, I.J., (2005). Comparison of inhomogeneity correction algorithms in small photon fields. *Medical physics*, 32(3), pp.766-776.
14. Knöös, T., Nilsson, M. and Ahlgren, L., (1986). A method for conversion of Hounsfield number to electron density and prediction of macroscopic pair production cross-sections. *Radiotherapy and Oncology*, 5(4), pp.337-345.
15. Kurudirek, M., (2014). Effective atomic numbers and electron densities of some human tissues and dosimetric materials for mean energies of various radiation sources relevant to radiotherapy and medical applications. *Radiation Physics and Chemistry*, 102, pp.139-146.
16. Ma, C., Cao, J., Yin, Y. and Zhu, J., (2014). Radiotherapy dose calculation on KV cone-beam CT image for lung tumor using the CIRS calibration. *Thoracic Cancer*, 5(1), pp.68-73.
17. Mohammadi, G.F., Alam, N.R., Rezaeejam, H., Pourfallah, T.A. and Zakariaee, S.S., (2015). Assessment of target volume doses in radiotherapy based on the standard and measured calibration curves. *Journal of Cancer Research and Therapeutics*, 11(3), pp.586-591.
18. Parker, R.P., Hobday, P.A. and Cassell, K.J., (1979). The direct use of CT numbers in radiotherapy dosage calculations for inhomogeneous media. *Physics in Medicine & Biology*, 24(4), p.802
19. Rhee, D.J., Kim, S.W., Jeong, D.H., Moon, Y.M. and Kim, J.K., (2015). Effects of the difference in tube voltage of the CT scanner on dose calculation. *Journal of the Korean Physical Society*, 67, pp.123-128.
20. Saini, A., Pandey, V.P., Kumar, P., Singh, A. and Pasricha, R., (2021). Investigation of tube voltage dependence on CT number and its effect on dose calculation algorithms using thorax phantom in Monaco treatment planning system for external beam radiation therapy. *Journal of Medical Physics*, 46(4), pp.315-323.

21. Saw, C.B., Loper, A., Komanduri, K., Combine, T., Huq, S. and Scicutella, C., (2005). Determination of CT-to-density conversion relationship for image-based treatment planning systems. *Medical Dosimetry*, 30(3), pp.145-148.
22. Seco, J. and Evans, P.M., (2006). Assessing the effect of electron density in photon dose calculations. *Medical physics*, 33(2), pp.540-552.
23. Sherouse GW, Chaney EL. The portable virtual simulator. *Int J Radiat Oncol Biol Phys.* (1991) Jul;21(2):475-82. doi: 10.1016/0360-3016(91)90799-a. PMID: 2061124.
24. Sontag, M.R. and Cunningham, J.R., (1978). The equivalent tissue-air ratio method for making absorbed dose calculations in a heterogeneous medium. *Radiology*, 129(3), pp.787-794.
25. Stergiopoulos, S., (2003). Advanced signal processing handbook: theory and implementation for radar, SONAR, and medical imaging real-time systems. *Medical Physics*, 30(5), p.995
26. Yamada, S., Ueguchi, T., Ogata, T., Mizuno, H., Ogihara, R., Koizumi, M., Shimazu, T., Murase, K. and Ogawa, K., (2014). Radiotherapy treatment planning with contrast-enhanced computed tomography: feasibility of dual-energy virtual unenhanced imaging for improved dose calculations. *Radiation oncology*, 9(1), pp.1-10.
27. Zhang, G.S., Huang, S.M., Chen, C., Xu, S.K., Zhang, D.D. and Deng, X.W., (2014). Evaluating the therapeutic dose distribution of intensity-modulated radiation therapy for head and neck with cone-beam computed tomography image: a methodological study. *BioMed research international*, 2014.

Incorporation of Wood ash and waste glass powder in enhancing concrete block performance

P V T Prarthana¹, R C L De Silva², P Subramaniam², S Thuraisingam³, J Prabagar⁴

¹Department of Physics, University of Sri Jayewardenepura, Sri Lanka.

² Industrial Technology Institute, Colombo 7, Sri Lanka.

³ Palmyrah Research Institute, Sri Lanka

⁴Department of Chemistry, University of Jaffna, Jaffna, Sri Lanka.

ABSTRACT

This study explores the feasibility of utilizing wood ash and waste glass powder as sustainable alternatives in the production of concrete blocks, aiming to address environmental concerns and enhance durability in construction. Cement blocks with varying percentages of wood ash (ranging from 10% to 25%) and a consistent 10% substitution of fine aggregates with waste glass powder were investigated. Six sample sets, including standard blocks, underwent testing for compressive strength, water absorption, and heat release at 7, 14, and 21 days of curing. Results demonstrate that a 15% wood ash replacement significantly improves compressive strength and reduces water absorption after 21 days. Furthermore, the combination of 15% wood ash with 10% glass powder replacement yields cement blocks with superior properties. The integration of wood ash with waste glass powder further enhances the performance of concrete blocks. By incorporating these materials into concrete block production, significant steps can be made towards reducing environmental impact and promoting sustainability within the construction industry.

Key Words: wood ash, waste glass powder, eco-friendly, concrete blocks, compressive strength

INTRODUCTION

The concrete blocks are widely used around the world including Sri Lanka for the construction of wall and buildings. Due to the low affordability of cement, and its adverse environmental effects the greener technology innovation is urged to use in developing construction material. The usage of supplementary materials to balance the portion of cement blocks is a beneficial for the field of construction. Lightweight materials have gained attention for their ease of use (Gunasekara et al., 2011). There are some crucial physical parameters such as strength, durability and workability considered in the preparation of concrete blocks in accordance with Portland cement properties. Many other studies revealed in cement manufacturing as the supplementary materials. Wood ash, rice husk and coconut shells are partially replaced of the cement (Antiohos et al., 2014; Udoeyo et al., 2006). It has proved that wood ash can be used to replace cement material partially in concrete production and it provides self-compact in construction field (Elinwa and Mahmood, 2002; Elinwa et al. 2008; Abdullahi, 2006). Particulate matter in wood fly ash are very irregular shape and higher number of pores in the surface (Wanget al. 2008). Physicochemical and structural properties of wood ash can affect the pozzolanic and hydraulic reactivity. The materials such as silica fume and fly ash (Islam et al., 2011; Imbabi et al., 2012) are used to improve the strength and workability of concrete blocks (Detwiler et al., 1996). Similarly, waste glass powder, a solution for colored glass waste, improves material properties (Du, & Tan 2014, Taha and Nounu, 2009). Even though, glass powder has not achieved at the commercialization level (Rashed, 2014). Glass contains the chemical components as supplementary cement materials (Ryou et al., 2006; Nassarand Soroushian, 2012). This research explores wood ash and waste glass powder to create eco-friendly concrete block material, aiming to reduce environmental impact while maintaining quality construction.

METHODOLOGY

Preparation of concrete blocks

Concrete blocks were prepared according to ASTM C109/C109M standards using wooden molds and colored glass powder. Wood ash from household kitchen and waste colored glass were collected as main raw materials. The kitchen ash underwent sieving through an 850-micrometer sieve to ensure consistent particle size, while colored glass was crushed into a fine powder and sieved through a 1.18 mm sieve.

Table 1: Concrete preparation design

Sample	Cement (%)	Ash (%)	Sand (%)	Glass powder (%)
1 (Control)	100	0.00	100	0.00
2 (Control)	100	0.00	90	10
3	90	10	90	10
4	85	15	90	10

5	80	20	90	10
6	75	25	90	10

A total of six concrete samples were prepared, with the first two serving as control samples. A 1:6 cement-to-sand ratio is used traditionally for the preparation of concrete blocks. Sample 1 followed the preparation method, while control sample 2 included 10% waste glass powder replacing sand for the subsequent samples. Ash replacement for cement and glass powder replacement for sand were indicated in the Table 1 as the percentage. A constant 10% of sand was replaced with waste glass powder, while the percentage of wood ash replacement for cement varied from 10% to 25%. Materials were mixed, then water was added, and thorough mixing for 10 minutes ensured homogeneity. The mixture was poured into molds and allowed to set for an hour. After an initial 24-hour room temperature cure, blocks were submerged in water until testing at 7, 14, and 21 days. Compressive strength, water absorption, and heat release tests were conducted to assess mechanical properties and performance, with results compared to control samples to evaluate the effectiveness of wood ash and waste glass powder in enhancing sustainability and mechanical strength.

Physical properties of concrete block

Compression strength

The prepared concrete blocks were dried for 24 hours after taking out from the water bath. The concrete block's compressive strength was investigated using a compressive strength testing machine at different curing days of 7, 14 and 21 days for each blocks. The mean value was calculated.

Water absorption

Water absorption testing was conducted for six prepared blocks, including the control samples (1 and 2). The selected sample blocks were kept in oven for 24 hours at $103 \pm 2^\circ\text{C}$ until their weight became constant, and their dry weights (w_1) were taken. Next, the same blocks were dipped in water bath for 24 hours, and their wet weights (w_2) were taken. The water absorption percentage of the block was calculated according to the below mentioned equation:

$$\text{Water Absorption \%} = \frac{(w_2 - w_1)}{w_1} \times 100 \quad (1)$$

Heat Release Test

The heat releasing test was conducted using an infrared (IR) thermometer. A sample block from each set was kept in an oven at $103 \pm 2^\circ\text{C}$ for a duration of 24 hours. Within the first hour of removal from the oven, the surface temperature of the sample block was measured at 5-minute intervals using the IR thermometer. By plotting the surface temperature against time, the rate of heat release was computed.

RESULTS AND DISCUSSION

Compression strength

The compressive strengths of concrete blocks were evaluated at various curing times, as presented in Table 2. The data illustrates a notable increase in compressive strength values for all samples with the progression of curing time (Figure 1). After curing of 21 days, the highest compressive strength is achieved when utilizing 15% wood ash and replacement in the cement and 10 % of sand was replaced by waste glass powder, displayed notably higher compressive strength compared to Sample 1, indicating the positive influence of glass powder incorporation.

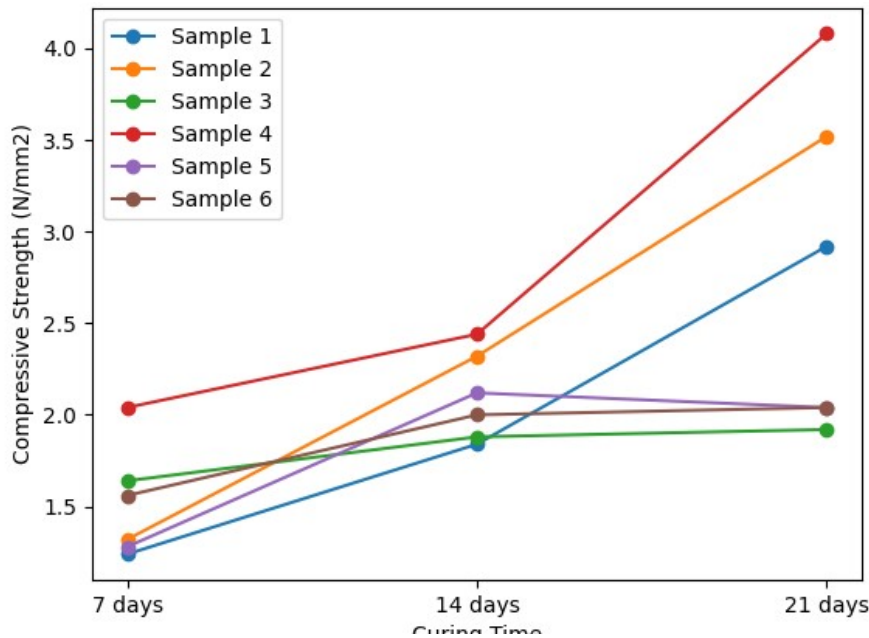


Figure 1: Compression Strength versus Curing Time

Glass incorporated into concrete can exhibit two distinct behaviors, the alkaline-silica reaction (ASR) and the pozzolanic reaction, each affecting concrete differently (Fengyan et al., 2006). ASR can lead to internal stresses, cracks, and structural damage, whereas the pozzolanic reaction, as observed in our study by replacing 10% of the sand with waste glass powder, enhances mechanical properties like compressive strength and durability.

For wood ash replacement, Sample 4, with a 15% ash replacement, demonstrated the most substantial rise in compressive strength compared to the control samples (Sample 1 and 2). This improvement was attributed to the pozzolanic reaction of wood ash, driven by its potassium, magnesium, and calcium content (Subramaniam et al., 2015).

The extensive surface area of wood ash particles facilitated a more extensive pozzolanic reaction, resulting in additional calcium silica hydrate gel formation. This not only improved the binding within the concrete matrix but also contributed to enhanced compressive strength, emphasizing wood ash as a sustainable cement replacement. Moreover, wood ash's presence positively influenced the concrete's pH, further enhancing its pozzolanic activity and, consequently, chemical resistance and durability. It's important to note that the compressive strength results after 21 days varied with different ash replacement percentages,

suggesting an optimal replacement level to balance the benefits of the pozzolanic reaction (Fengyan et al., 2006).

Water Absorption Test

The water absorption capability of concrete blocks in 7, 14 and 21 days are given in Table 2. The results indicated that the water absorption ability of all blocks except sample 6 are much less compared to control blocks after the curing period of 21 days. The lowest absorption ability was found to be in sample 4.

Table 2: Water absorption percentage over different curing time

Sample	Water Absorption Percentage (%)		
	7 Days	14 Days	21 Days
1 (Control)	9.36	7.68	8.32
2	7.1	6.07	7.29
3	6.45	6.49	6.17
4	7.42	6.16	6.1
5	6.11	7.35	7.24
6	7.91	9.5	9.18

Heat Release Test

The findings regarding the heat release rate with varying percentages of included materials at different curing days are presented in Figure 2. Notably, on the 21st day of curing, sample 3, 4, 5, and 6 exhibited lower heat release rates when compared to the control samples. Among these, sample 5 demonstrates the lowest heat release rate after 21 days, while sample 4 displays the second lowest heat release rate during the same period.

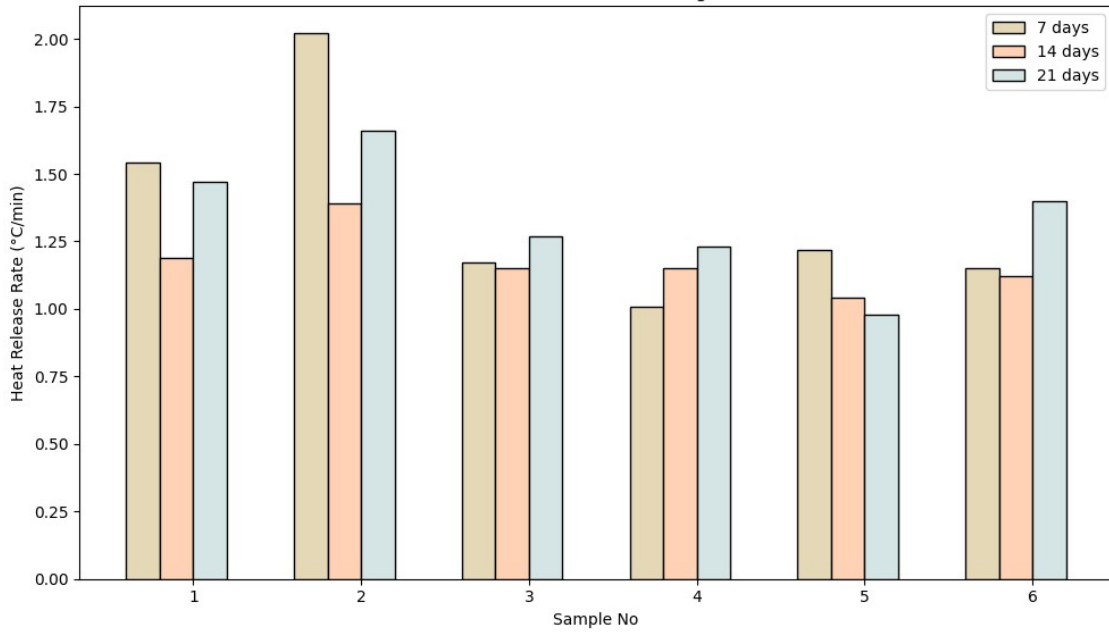


Figure 2: Heat release rate of samples over curing time

Concrete's water absorption characteristics significantly impact its durability (Ithuralde, 1992). In comparison to the control samples, all concrete samples containing wood ash demonstrated relatively lower heat release rates, contributing to enhanced thermal comfort in various settings

Comparison of wood ash and glass powder incorporated concrete

Wood ash (WA) and glass powder (GP) incorporated in concrete blocks is a commercially beneficial in the construction industry. It is used as filler which enhances cement properties and increase the economic benefits of concrete.

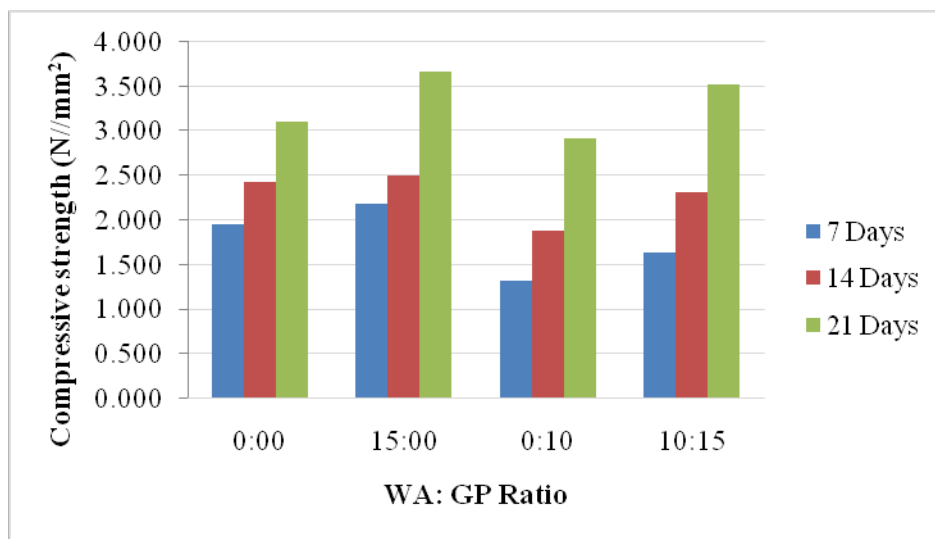


Figure 3: Compressive strength of samples over curing time

Table 3 presents the compressive strengths of cement with the partial replacement of waste glass powder and wood ash after 21 days of curing. According to the statistical analysis (Turkey HSD, $p < 0.05$) there was no significant difference in compressive strengths between the samples with 15% wood ash addition and those with a 10:15 ratio of glass powder to wood ash addition. These compositions exhibited high results, ranging from 3.58 to 3.69 N/mm², compared to the control cement. These values meet the minimum requirement of 2.8 N/mm² specified in BS 6073: Part 2: 1981. Previous studies have also demonstrated similar trends, where cement with 10% glass powder showed the highest compressive strength (Rashed, 2014), while contrasting findings indicated that 20% addition of glass powder yielded higher compressive strength at 90 days (Sadiqul Islam et al., 2017).

Table 3: Comparison of physical properties of 21 Days cured concrete

Concrete	Strength/ (N/mm ²)	Water absorption	Heat releasing rate
WA:GP	21 Days	21 Days	21 Days
00:00	3.073 ± 0.052 ^b	8.365 ± 0.058 ^d	0.978 ± 0.011 ^a
15:00	3.689 ± 0.056 ^a	9.662 ± 0.074 ^c	0.953 ± 0.011 ^a
00:10	2.923 ± 0.005 ^c	7.293 ± 0.007 ^b	1.663 ± 0.005 ^b
10:15	3.587 ± 0.057 ^a	6.152 ± 0.052 ^a	0.977 ± 0.005 ^a

Means that do not share a letter are significantly different.

The concrete with a 15:10 ratio of wood ash to glass powder exhibited lower permeability, attributed to the effective filling of pores by both ash and glass powder. This feature is desirable as it minimizes concrete deterioration. Regarding heat release properties, significant differences were only observed in concrete incorporating 10% glass powder ($P < 0.05$). Concrete containing 15% wood ash and a 15:10 ratio of wood ash to glass powder displayed a similar and gradual heat release pattern. This characteristic is crucial for maintaining thermal comfort.

CONCLUSION

The inclusion of waste glass powder and wood ash in concrete block preparation has yielded favourable outcomes on mechanical properties. Specifically, the combination of 15% wood ash and 10% glass powder replacement has led to cement blocks exhibiting increased compressive strength and reduced water absorption capacity following 21 days of curing. Moreover, the incorporation of wood ash alongside glass waste powder has contributed to moderating the rate of heat release, despite the inherent tendency of glass material to release heat rapidly. Collectively, these findings underscore the potential of both waste glass powder and wood ash as sustainable alternatives for enhancing the properties of cement-based materials in various construction applications.

REFERENCES

1. Abdullahi M. (2006). Characteristics of wood ash/OPC concrete. *Leonardo Electronic Journal of Practices and Technologies* 8:9–16.
2. Antiohos S.K, Papadakis V.G, Tsimas S. (2014). Rice husk ash (RHA) effectiveness in cement and concrete as a function of reactive silica and fineness. *Cement and Concrete Research*. (61-62) 20-27.

3. ASTM C109, 2016c. Standard Test Method for Compressive Strength of Hydraulic Cement Mortars (Using 2-in. or [50-mm] Cube Specimens). ASTM International, West Conshohocken, USA.
4. Detwiler, R., Bhatti, J.I., Bhattacharja, S., 1996. Supplementary Cementing Materials for Use in Blended Cements. Research and Development Bulletin Rd112t, Portland Cement Association, Skokie, Illinois, USA.
5. Du, H., & Tan, K. H. (2014). Waste glass powder as cement replacement in concrete. *Journal of Advanced Concrete Technology*, 12(11), 468-477.
6. Elinwa AU, Ekeh SP, Mamuda AM. Assessing of the fresh concrete properties of self-compacting concrete containing sawdust ash. *Construction and building materials* 2008; 22:1178–82.
7. Elinwa AU, Mahmood YA. 2002. Ash from timber waste as cement replacement material. *Cement and Concrete Composites* 24:219–22.
8. Fengyan, W., Xianghui, L., Yinong, L., & Zhongzi, X. (2006). Effect of pozzolanic reaction products on alkali-silica reaction. *Journal of Wuhan University of Technology-Mater. Sci. Ed.*, 21, 168-171.
9. Gunasekaran, K., Kumar, P. S., & Lakshmiopathy, M. (2011). Mechanical and bond properties of coconut shell concrete. *Construction and Building Materials*, 25(1), 92-98.
10. Imbabi, M.S., Carrigan, C., McKenna, S., 2012. Trends and developments in green cement and concrete technology. *Int. J. Sustain. Built Environ.* 1, 194–216.
11. Islam, G.M.S., Islam, M.M., Akter, A., Islam, M.S., 2011. Green construction materials-Bangladesh perspective. In: *Proceedings of the International Conference on Mechanical Engineering and Renewable Energy 2011, (ICMERE2011) 22–24 December 2011, Chittagong, Bangladesh (ID-063)*.
12. Ithuralde, G. (1992). Permeability: The Owner's Viewpoint. In: Mailer Y. ed. *High-Performance Concrete from Material to Structure*. London: 276-294.
13. Nassar, R.U.D., Soroushian, P., 2012. Strength and durability of recycled aggregate concrete containing milled glass as partial replacement for cement. *Constr. Build. Mater.* 29, 368–377.
14. Rashed, A.M., 2014. Recycled waste glass as fine aggregate replacement in cementitious materials based on Portland cement. *Constr. Build. Mater.* 72, 340–357.
15. Ryou, J., Shah, S.P., Konsta-Gdoutos, M.S., 2006. Recycling of cement industry wastes by grinding process. *Adv. Appl. Ceram.* 105, 274–279.
16. Sadiqul Islam, G.M., Rahman, M. H. and Nayem Kazie. (2017). *International Journal of Sustainable Built Environment*. 6.37–44
17. Subramaniam, P., Subasinghe, K., & Fonseka, W. K. (2015). Wood ash as an effective raw material for concrete blocks. *International Journal of Research in Engineering and Technology*, 4(2), 2319-1163.
18. Taha, B., Nounu, G., 2009. Utilizing waste recycled glass as sand/cement replacement in concrete. *J. Mater. Civ. Eng.* 21 (12), 709–721
19. Udoeyo FF, Inyang H, Young DT, Oparadu EE. 2006. Potential of wood waste ash as an additive in concrete. *Journal of Materials in Civil Engineering* 18(4):605–11
20. Wang S, Baxter L, Fonseca F. 2008. Biomass fly ash in concrete: SEM, EDX and ESEM analysis. *Fuel* 87:372–9.

Low-Pressure and Atmospheric-Pressure Cold Plasma Treatment as a Pretreatment for Extracting Volatile Oils from Black Pepper (*Piper nigrum*) Seeds

A B G C J De Silva¹, H D Weerathunge¹, P N R J Amunugoda^{1*}, S H P Gunawrdena², A A P de Alwis²

Industrial Technology Institute, Sri Lanka¹

Department of Chemical and Process Engineering, University of Moratuwa, Sri Lanka²

ABSTRACT

Volatile Oils (VOs) are essential contributors to the aroma and flavor of black pepper seeds, making their analysis crucial after sterilization processes. This study aimed to qualitatively and quantitatively analyze VOs in black pepper seeds that have been subjected to the following two modes of Cold Plasma (CP) treatments to evaluate its efficacy as a pretreatment for hydro distillation. CP generating setups, Low-Pressure Cold Plasma (LPCP) and Gliding Arc Plasma Discharge (GAPD) were used for the study. A commercially available black pepper (*Piper nigrum*) variety (MB12) underwent CP treatments with varying time durations (5, 10, and 15 minutes). The VOs were extracted using hydro-distillation and identified and quantified by GC-MS and GC-FID respectively. The study examined 12 major components of VOs, including α -pinene, β -caryophyllene, and D-limonene. Results revealed that LPCP at 5 minutes and GAPD at 10 minutes yielded the highest VO content, while prolonged treatment times led to decrease oil yields in both treatments. No significant differences were observed in individual VO components between the two CP treatments. The refractive index of VOs after LPCP and GAPD treatments did not significantly differ, affirming the GC-FID results. Importantly, the study concluded that both 5-minute treatment time of LPCP and 10-minute treatment time of GAPD did not adversely affect the quality of VOs in black pepper seeds. The results of the study highlighted the necessity of insights into optimal processing conditions and highlighting the utility of LPCP and GAPD as pretreatments for VO extraction.

Keywords: black pepper seeds, volatile oils extraction, cold plasma, gliding arc plasma, low pressure plasma

INTRODUCTION

The distinctive flavor and aroma of black pepper are attributed to its essential oil, constituting approximately 3–6% of the black pepper (*Piper nigrum*) (Pepper *et al.*, 2019). The composition of volatile oil content depends upon the maturity and are reported as 8.6 ml/100g at 22.5 weeks mature in Sri Lankan black pepper and the volatile oils are contained in the inner layers of the mesocarp (Jansz *et al.*, 1984). Due to the significant economic and medicinal importance of volatile oils of black pepper seeds, numerous studies have been conducted to explore the methods of volatile oil extraction and characterization. The oil, ranging from colorless to greenish, emanates a spicy (peppery) fragrance. Extraction methods such as distillation, simultaneous distillation-extraction (SDE), solid phase microextraction (SPME), or supercritical fluid extraction are commonly employed to obtain black pepper oil from *P. nigrum* fruits (Can Başer & Buchbauer, 2015; Pepper *et al.*, 2019). Nevertheless, these approaches come with certain drawbacks, such as an extended extraction duration, substantial energy consumption, potential contamination by solvents, the necessity for supplementary purification steps, and an adverse impact on the caliber of extracts and overall amount of extracted material (Alashti *et al.*, 2024). The process of hydro-distillation stands as the oldest and frequently employed technique for obtaining aromatic essences such as volatile oils from botanical substances. This method holds distinct advantages over alternative extraction techniques, as the equipment is cost-effective and straightforward to construct, simple to use and feasible for mass production. Consequently, it finds extensive utilization within the essential oil industry (Do, 2022). Therefore, a pretreatment to increase the oil extraction yield coupled to hydro-distillation is a timely requirement.

The potential of cold plasma technology for diversified applications in the food industry such as microbial decontamination, increasing seed germination yield and producing plasma activated water are being experimented worldwide (Adamovich *et al.*, 2022; Afshari & Hosseini, 2014; Cherif *et al.*, 2023; Chizoba Ekezie *et al.*, 2017) and is now being assessed as a pretreatment for drying (Loureiro *et al.*, 2021; Shishir *et al.*, 2020; Tabibian *et al.*, 2020) and extraction (Heydari *et al.*, 2023; Kodama *et al.*, n.d.). Cold plasma is generated through the electrical breakdown of gases at varying pressure gradients (ranging from low pressure to atmospheric pressure), resulting in a gas that is partially or fully ionized (Shishpanov *et al.*, 2020; Ansari *et al.*, 2022; Chizoba Ekezie *et al.*, 2017). The makeup of cold plasma is distinctively determined by the setup and operational parameters, including the power source, voltage, frequency, pressure circumstances, gas composition, and environmental factors (Valencia *et al.*, 2022). In contemporary research, a variety of methods for generating cold plasma are employed, including low-pressure cold plasma glow discharge, dielectric barrier discharge, atmospheric plasma jet, corona discharges, gliding arc discharge, and plasma torch (Chiappim *et al.*, 2023; Misra *et al.*, 2011; Thirumdas *et al.*, 2017b; Yang *et al.*, 2024). Cold plasmas, commonly known as non-equilibrium plasmas exhibit distinctive temperature variations among plasma species (Akishev *et al.*, 2010; Kogelschatz, 2003; Kuzminova *et al.*, 2017; Misra *et al.*, 2016). Within cold plasma, the electron temperature remains unbalanced with the resultant ion temperature, even though the supplied energy is sufficient to sustain electron flow and induce partial ionization of the gas. The generation of cold plasma is achievable under both low-pressure and atmospheric pressure conditions (Sarangapani *et al.*, 2015). Non-equilibrium plasma persists across a spectrum of

pressures, typically spanning from approximately 0.1 to 100 Pa for low-pressure plasma, or at atmospheric pressure (around 10^5 Pa).

A pivotal contrast lies in the behaviour of reactive gaseous species between low-pressure and atmospheric-pressure plasmas, notably in their lifespans. Reactive species often endure for mere microseconds at atmospheric pressure but can extend beyond a second under low pressure. At atmospheric pressure, predominant loss mechanisms involve homogeneous reactions in the gas phase, while at low pressure, varied reactions in the surface dominate (Primc, 2022).

Nevertheless, cold plasma, as a surface treatment method, exhibits restricted penetration depth, influenced by factors such as substrate structure and composition, power input, distance between the plasma source and the surface, as well as the half-lives of reactive species (Hertwig *et al.*, 2018). Recent studies have shown penetration depths in various biofilms ranging from 1 nm to 50 μ m, reaffirming the efficacy of cold plasma technology in surface treatment (Bußler, n.d.; Ziuzina, 2015).

Plasma has wide applications in removing of materials in nano - micro levels which is referred to as "etching". During cold plasma treatment surface etching is one of the key phenomena occur by physical sputtering or chemical reactions in material processing industry. Plasma etching, reactive ion etching and sputtering etching are the key types of etching processes which are referred related to the mode of action (Thirumdas *et al.*, 2017b). Different commercial surface modifications such as increasing hydrophilicity, hydrophobicity and functionalization are carried out with specific plasma designs in polymer, plastic and metal industries (Chizoba Ekezie *et al.*, 2017; Fitzpatrick *et al.*, 2016; Sarangapani *et al.*, 2016; Submitted *et al.*, 2011; Thirumdas *et al.*, 2017a). However, the phenomenon is widely applicable in the food industry as a surface treatment method especially as a pretreatment method (Annor *et al.*, 2014; H. S. Lee *et al.*, 2020; Yu *et al.*, 2014).

The extraction yield of plant components is subject to various factors, encompassing the extent of cell wall disruption, plant/botanical species, surfaces, and the chemical makeup of active biological compounds inherent to the plant. Cold plasma processes have been shown to induce alterations in the physical properties of different plant matrices especially in the surfaces. This results in the development of fissures and indentations on the surface cracks, facilitating an enhanced exudation of substances and thereby elevating the extraction yield (Heydari *et al.*, 2023). For the utilization of atmospheric pressure plasma in material processing, in etching and deposition applications, the necessity extends beyond achieving a uniformly distributed plasma over a large area and need to have a high plasma density (Y. H. Lee & Yeom, 2005).

With that background, the study was intentional to investigate the potential of low-pressure and atmospheric pressure cold plasma technology to use as pretreatment methods to extract volatile oils from black pepper seeds using hydro-distillation.

METHODOLOGY

Sample Selection

Samples of black pepper seeds, weighing 100g each and meeting export quality standards, were acquired from a processing facility specializing in black pepper in Padukka, Western Province, Sri Lanka. The facility processes the MB12 variety of black pepper cultivated in Matale, Central Province, Sri Lanka. The diameters of 100 black pepper seeds were measured individually using a calibrated Vernier caliper (GENERAL, USA). The chosen black pepper seeds for the study have a mean diameter of 4.72 ± 0.39 mm and an average mass of 0.053 ± 0.013 g.

Cold plasma treatment for black pepper seeds

Two cold plasma generating setups, Low-Pressure Cold Plasma treatment (LPCP) and Gliding Arc Plasma Discharge (GAPD) were used for the study (Figure 02 (a) and (b)). The descriptive methods carried out for each treatment are described below.

Low Pressure Cold Plasma Treatment

Utilizing a 300 W, 30 L low pressure plasma chamber operating at radio frequency in a plasma setup with parallel plate capacitance coupling, the Low-Pressure Cold Plasma Treatment (depicted in Figure 02 (b)) was executed. Oxygen, with a purity of 99.99%, served as the treatment gas. The black pepper seeds sample was evenly distributed in a metal tray with a rectangular shape with a packing seeds density of 0.22 g/cm² (250 mm x 150 mm), strategically placed at the central point within the low-pressure chamber. To regulate the process, the oxygen gas supply rate was maintained at 120 cm³/min, ensuring a pressure range between 0.35 mbar and 0.45 mbar. The treatment parameters included a wattage setting of 250 W, and treatment durations of 5, 10, and 15 minutes.

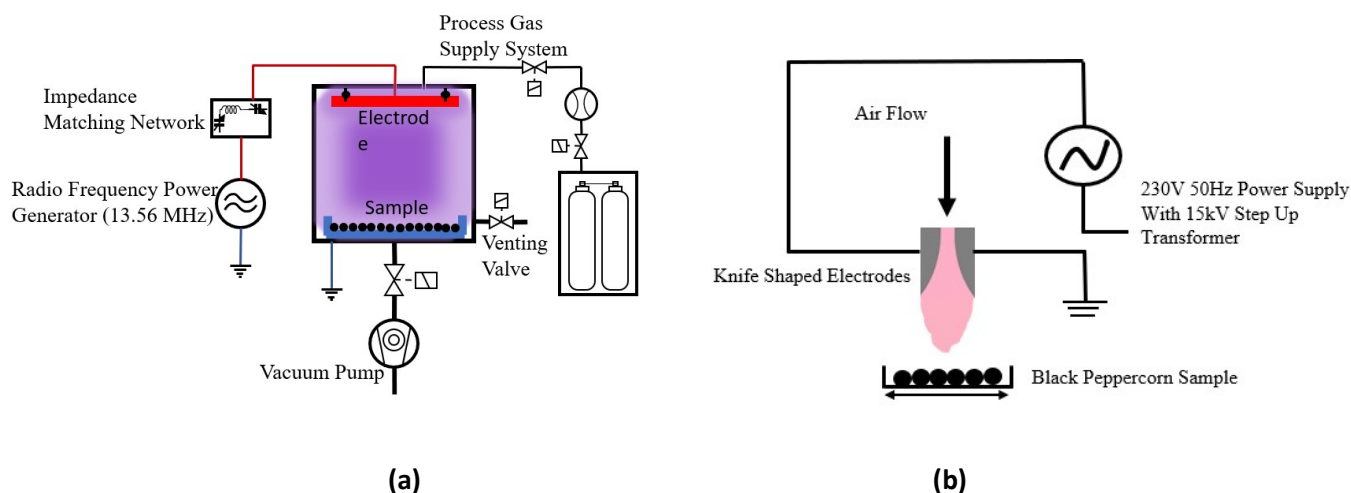


Figure 1: (a) Low Pressure Cold Plasma Treatment (b) Gliding Arc Plasma Discharge Treatment

Gliding Arc Plasma Discharge Treatment

The study employed a Gliding Arc Plasma Discharge system procured from Eltech Pvt Ltd in Mumbai, India. Cold plasma, generated at a fixed supply voltage of 15 kV and Alternating Current at 50 Hz, utilized

atmospheric air with a flow rate of 0.009 m³/s. In the experimental setup, 20g of pepper seeds sample was evenly dispersed as a single layer of black pepper seeds (0.22 g/cm²) in a petri dish and it was placed in a holder made up of poly acrylic acid. The holder with the petri dish having black pepper seeds was placed 4 cm below the plasma discharge. Manual horizontal shaking was done wearing electrically insulated gloves twice a minute. The study operated under atmospheric conditions with air at 26°C and 65% humidity. Treatment durations were established at 5 minutes, 10 minutes, and 15 minutes, each repeated three times for analysis.

Volatile Oil Extraction

To obtain pepper seed oils in accordance with AOAC 17th edition 2000, 962.17, hydro-distillation was conducted with a sample size of three (n=3). The process involved crushing 50 g of pepper seeds in a dry grinder for five seconds, followed by heating the crushed seeds with distilled water amounting 500 ml. The vapor generated during this process was underwent condensation and refluxing for about 4 hours until the oil collected in the trap had no alteration in the volume in one-hour time interval. Subsequently, the amount of volatile oil accumulated in the trap was quantified using a calibrated measuring cylinder. The amount of oil extracted was determined using the following equation (Equation 1).

$$\text{Volatile Oil Content} = \frac{\text{Volume of oils extracted in the hydrodistillation unit (ml)}}{\text{Dried weight of crushed black pepper used (g)}} \dots (1)$$

Analysis of Volatile Oils by Gas Chromatography – Mass Spectroscopy

Volatile oil in black pepper seeds was both identified and quantified through Gas Chromatography-Mass Spectrometry (GC-MS) and Gas Chromatography with Flame Ionization Detection (GC-FID), respectively. Qualitative analysis of the volatile oil was conducted using a Gas Chromatograph (Thermo Scientific TRACE 1300) coupled with a Mass Spectrometer (ISQ-QD, Single Quadrupole). This setup included an auto injector AI 1310 (Thermo Scientific) and a Thermo Scientific fused silica capillary column (DB-WAX UI) measuring 30 m × 0.25mm i.d., with a 0.25 μm film. Helium was used as the carrier gas at a flow rate of 1.0 ml/min. The temperature program was set as follows: initial temperature at 60°C, with a ramp of 5°C min⁻¹ up to 220°C. The injector temperature was maintained at 240°C, and the ion source temperature at 250°C. 0.3 μl of oil samples, diluted with 1 ml of hexane, were injected with a split ratio of 1:50 and a column pressure of 64.20 kPa. Mass Spectrometry was conducted using an ion capture detector with an impact energy of 70 eV. Constituent identification relied on comparing mass spectra with those in the equipment database (NIST11) and the library (Wiley Registry of Mass Spectral Data, 10th Edition, 2015). Retention indices for each identified component were determined using a C7-C30 saturated alkane standard (SUPELCO) at a concentration of 1000 μg/ml in hexane.

Analysis of Volatile Oils by Gas Chromatography – Flame Ion Detection

Each constituent's quantification was established through Gas Chromatographic analysis with Flame Ionization Detector (FID) using area normalization (%) method. The proportional concentrations of the identified oil components were derived through peak area normalization, where the total peak area served as the reference set at 100%. The proportion of each constituent was calculated based on the area of its

respective peak. To prepare the samples for analysis, the oil samples underwent filtration using micro filters. Subsequently, 1 ml of each filtered sample was carefully transferred to glass vials using a micro pipette. The samples were then subjected to vortex for approximately 60 seconds before injection into the analytical system.

Refractive Index of Volatile Oils

The Refractive Index of the volatile oils obtained through hydro-distillation was assessed using an OGAWA SEIKI Refractometer, employing the methodology outlined in ISO 6320:2017.

Statistical Analysis

Every analysis was conducted in triplicate. The impact of the treatment was evaluated for significant differences at a significance level of $P < 0.05$ using Minitab 14, employing ANOVA one-way analysis. Differences between means were assessed through a two-sample T-test at a 95% confidence level. Differences between means were further elucidated using Tukey's test at a significance level of $p < 0.05$.

RESULTS AND DISCUSSION

The amount of volatile oil extracted and their refractive indices obtained after Low Pressure Cold Plasma (LPCP) and Gliding Arc Plasma Discharge (GAPD) treatments are depicted in Table 01. There is an increase in the volatile oils extracted from black pepper seeds when compared to the untreated sample in LPCP treatment.

The LPCP treatment was carried out in a low-pressure chamber where the pressure inside the chamber is 0.3 – 0.5 mbar. Moreover, more uniform treatment can be expected in the LPCP with the glow type uniform plasma discharge inside the LPCP chamber throughout the treatment. When black pepper seeds are exposed to plasma within the LPCP chamber, reactive species function to strip off or remove material from the surface more uniformly than in the GAPD treatment, creating channels that allow escaping of volatile oils. As depicted in Table 1, 5-minute treatment time had the highest volatile oil extraction yield confirming that 5-minute treatment was capable to facilitate the hydro distillation process increasing the volatile oil content by 24.1 %. Further treatments reduced the oil extraction yields and the very low pressure in the surrounding (LPCP chamber) might support the evacuation of volatile oils faster than in the GAPD which was carried out under atmospheric pressure conditions. Supporting to this, similar alteration of volatile oils were detected in treating lemon verbena and the research revealed that the alteration of the surface properties through cold plasma treatment made the development of porous surface, facilitating the easy extraction or release of volatiles from lemon verbena (Ebadi, 2019).

In GAPD treatment, the highest oil extraction yield was found after 10 minutes treatment and the sample treated for 15 min detected a reduced oil extraction when compared to 10-minute treatment. It was observed that 10 min of GAPD treatment enhanced the volatile oil extraction content by 27.6 %.

Table 1: Volatile Oil Extraction and Refractive Index of Volatile Oils after Cold Plasma Treatments

Treatment	LPCP		GAPD	
	Oil Extraction (ml/g)	Refractive Index	Oil Extraction (ml/g)	Refractive Index
Control	0.029 ± 0.001 ^a	1.4851 ± 0.0029 ^a	0.029 ± 0.001 ^a	1.4851 ± 0.0029 ^a
5 min	0.036 ± 0.001 ^b	1.4836 ± 0.0008 ^a	0.032 ± 0.002 ^a	1.4849 ± 0.0006 ^a
10 min	0.029 ± 0.002 ^a	1.4839 ± 0.0007 ^a	0.037 ± 0.002 ^a	1.4870 ± 0.0008 ^a
15 min	0.028 ± 0.001 ^a	1.4840 ± 0.0009 ^a	0.032 ± 0.001 ^a	1.4829 ± 0.0010 ^a

Data is expressed as mean ± SEM, n = 3. Means followed by the different letters (a and b) indicate a significant difference at $p < 0.05$ between the data within the same columns

These increases of the volatile oil extractions after GAPD treatment arises an argument that GAPD treatment can facilitate the hydro-distillation process allowing more trapped oils in the internal structures of the black pepper seeds to come out, assisting the hydro-distillation process. In GAPD, the reactive species generated (with nitrogen, oxygen and water vapors etc.) in the plasma interact with the black pepper seeds' surface along with the plasma flow which comes through the electrodes. This continuous bombardment of plasma species, throughout time, etched the surface of black pepper seeds, forming microchannels to facilitate the extraction of volatile oils. After this continuous interaction reach to a threshold point, the volatile oil tends to release from the black pepper seeds surface with the forced air flow ($0.009 \text{ m}^3/\text{s}$) in the GAPD treatment. Therefore 10-minute treatment time was effective in obtaining the maximum volatile oil extraction. However, this optimum treatment time is specific to the amount of black pepper seeds used in this study and scaled up research are required for defining the batch sizes and treatment times to optimize the process. Complying with the increment of the volatile oils obtained, similar findings were obtained for lemon verbena and lemon peel resulting in loss of volatile oils (Ebadi, 2019). Moreover, the volatile oils extracted from citrus peels using Dielectric Barrier Discharge Plasma treatment of 30 kV, 50 Hz resulted in improving the extraction of oil yields confirming the results of this study (Kodama *et al.*, n.d.).

In order to obtain the highest volatile oil extraction yield, LPCP was effective within a comparatively short time than GAPD. However, when proceeding with the scaled-up research the investment cost and the operating cost have to be considered for the industrial applications, since the investment and operating cost of LPCP is costlier than for GAPD.

The refractive index of volatile oils extracted using both plasma treatments did not affect significantly reflecting consistence of the quality of volatile oils as can be seen in Table 01. The refractive indices obtained in this study comply with the previously obtained values of refractive indices of black pepper volatile oils (Setiawan *et al.*, 2019).

As Table 02 illustrates, 12 major components of volatile oils were identified and quantified from black pepper seeds. The identified volatile oils were, α -pinene, β -pinene, sabinene, δ -3-carene, β -myrcene, D-limonene, β -phellandrene, O-cymene, δ -elemene, α -copaene, β -caryophyllene and Caryophyllene Oxide. Each identified component is specific to a key feature in the aroma profile of the black pepper seeds. All the identified constituents except Caryophyllene and Caryophyllene Oxide were not changed statistically significantly ($P > 0.05$) though there are changes in the composition in many of the identified oil components after GAPD treatment. Caryophyllene content in extracted volatile oils decreased significantly ($P < 0.05$) after 15 min treatment, while Caryophyllene Oxide escalated after 15 min GAPD treatment which can lead to change the odor profile. Long exposure time together with the reactive oxygen species generated in plasma discharge can cause the oxidation of β -caryophyllene to Caryophyllene Oxide. This further confirmed that 10-minute treatment time of GAPD was the most appropriate time for facilitating the volatile oil extraction using hydro-distillation.

Similar to the GC-MS and GC-FID analysis carried out for the volatile oils extracted from the black pepper seeds after GAPD treatment, there was no statistical significance in the composition when twelve components of volatile oils are considered in LPCP treatment. However, as can be seen in Table 02, changes in composition were observed in volatile oils directing to change the quality of volatile oils. α -pinene, β -pinene, O-cymene, δ -3-carene and Caryophyllene Oxide were increased after LPCP treatments while, D-limonene, δ -elemene, α -copaene, and β -caryophyllene decreased after the treatments. Irrespective to the extracted volatile oils yield, slight changes of the composition with the LPCP treatment was observed.

The compositional analysis highlighted that, though the volatile oil extraction yield increased with the GAPD and LPCP treatments, no significant changes were detected composition wise confirming the applicability of the two methods for using as pretreatment methods.

Table 2: Variation of volatile oils with GAPD and LPCP Treatment

No:	Component	RI*	Control	GAPD			LPCP		
				5 min	10 min	15 min	5 min	10 min	15 min
1	α -pinene	932	21.34 \pm 2.06	20.84 \pm 1.22	21.56 \pm 0.98	23.24 \pm 0.12	24.05 \pm 0.18	24.78 \pm 0.09	22.79 \pm 1.60
2	β -pinene	1049	0.37 \pm 0.02	0.38 \pm 0.04	0.42 \pm 0.04	0.41 \pm 0.02	0.42 \pm 0.01	0.41 \pm 0.02	0.38 \pm 0.02
3	Sabinene	1062	12.82 \pm 0.66	12.66 \pm 0.43	12.48 \pm 0.73	13.02 \pm 0.07	12.77 \pm 0.14	13.03 \pm 0.08	12.68 \pm 0.19
4	δ -3-carene	1095	16.76 \pm 0.63	16.68 \pm 0.28	17.7 \pm 2.41	17.45 \pm 0.52	18.21 \pm 0.39	18.41 \pm 0.07	18.52 \pm 0.61
5	β -myrcene	1106	8.65 \pm 0.12	8.70 \pm 0.23	8.01 \pm 0.39	8.84 \pm 0.12	8.05 \pm 0.27	8.36 \pm 0.13	7.91 \pm 0.36
6	D-limonene	1141	2.41 \pm 0.09	2.42 \pm 0.05	1.98 \pm 0.16	2.48 \pm 0.02	2.17 \pm 0.05	2.00 \pm 0.05	2.15 \pm 0.02
7	β -phellandrene	1152	15.04 \pm 0.21	15.16 \pm 0.11	14.46 \pm 0.32	14.81 \pm 0.33	14.15 \pm 0.07	14.17 \pm 0.14	14.26 \pm 0.05
8	O-cymene	1214	0.58 \pm 0.02	0.58 \pm 0.04	0.61 \pm 0.03	0.75 \pm 0.05	0.63 \pm 0.06	0.68 \pm 0.06	0.66 \pm 0.03
9	δ -elemene	1462	0.41 \pm 0.02	0.44 \pm 0.04	0.42 \pm 0.12	0.45 \pm 0.15	0.32 \pm 0.06	0.30 \pm 0.02	0.35 \pm 0.03
10	α -copaene	1483	1.21 \pm 0.16	1.15 \pm 0.09	1.45 \pm 0.31	0.93 \pm 0.02	1.08 \pm 0.01	0.99 \pm 0.03	1.14 \pm 0.13
11	β -caryophyllene	1585	13.75 \pm 1.78	13.71 \pm 1.00	16.11 \pm 3.44	11.21 \pm 0.11	12.00 \pm 0.19	11.09 \pm 0.24	12.62 \pm 0.13
12	Caryophyllene Oxide	1969	0.47 \pm 0.11	0.45 \pm 0.05	0.15 \pm 0.30	0.36 \pm 0.03	0.55 \pm 0.01	0.61 \pm 0.09	0.52 \pm 0.03

* Retention Index Data is expressed as mean \pm SD, n = 3

Similar to the GC-MS and GC-FID analysis carried out for the volatile oils extracted from the black pepper seeds after GAPD treatment, there was no statistical significance in the composition when twelve components of volatile oils are considered in LPCP treatment. However, as can be seen in Table 02, changes in composition were observed in volatile oils directing to change the quality of volatile oils. α -pinene, β -pinene, O-cymene, δ -3-carene and Caryophyllene Oxide were increased after LPCP treatments while, D-limonene, δ -elemene, α -copaene, and β -caryophyllene decreased after the treatments. Irrespective to the extracted volatile oils yield, slight changes of the composition with the LPCP treatment was observed.

The compositional analysis highlighted that, though the volatile oil extraction yield increased with the GAPD and LPCP treatments, no significant changes were detected composition wise confirming the applicability of the two methods for using as pre-treatment methods.

Volatile oils of black pepper are predominantly composed of monoterpene hydrocarbons, constituting 30-70 % of the total. Examples include α -pinene, β -pinene, limonene, sabinene, myrcene, β -phellandrene, and δ -3-carene. Sesquiterpenes, particularly β -caryophyllene, contribute significantly to the volatile oil content, accounting for approximately 25-45 % of the total. Additionally, oxygen enriched sesquiterpenes like caryophyllene oxide are present in quantities ranging from 4-14 % (Schulz *et al.*, 2005).

The oils identified in this study primarily consisted of monoterpene hydrocarbons, aligning with findings from prior research (Pepper *et al.*, 2019). Figure 03 displays the monoterpenes, sesquiterpenes, and oxygenated compounds derived from volatile oils extracted from black pepper seeds pre- and post-treatment with GAPD and LPCP.

In GAPD treatment, there was no significant difference ($P > 0.05$) in monoterpenes content of the volatile oils and the sesquiterpene content significantly decreased after 15 min treatment. Monoterpene content varied in between 60 – 66 % while sesquiterpenes ranged from 28 – 32 % by weight complying to the available literature (Pepper *et al.*, 2019) even after exposing to the cold plasma treatment. Sesquiterpenes content decreased from 31.45 to 28.63 % and however the amount remaining after treatments was well within the typical ranges. These minor components of volatile oils create different and specific notes, contributing to the aroma profile of black pepper. As mentioned in the literature (Schulz *et al.*, 2005), achieving an ideal pepper aroma quality involves a high concentration of monoterpenes excluding α -pinene and β -pinene, coupled with a low level of pinenes.

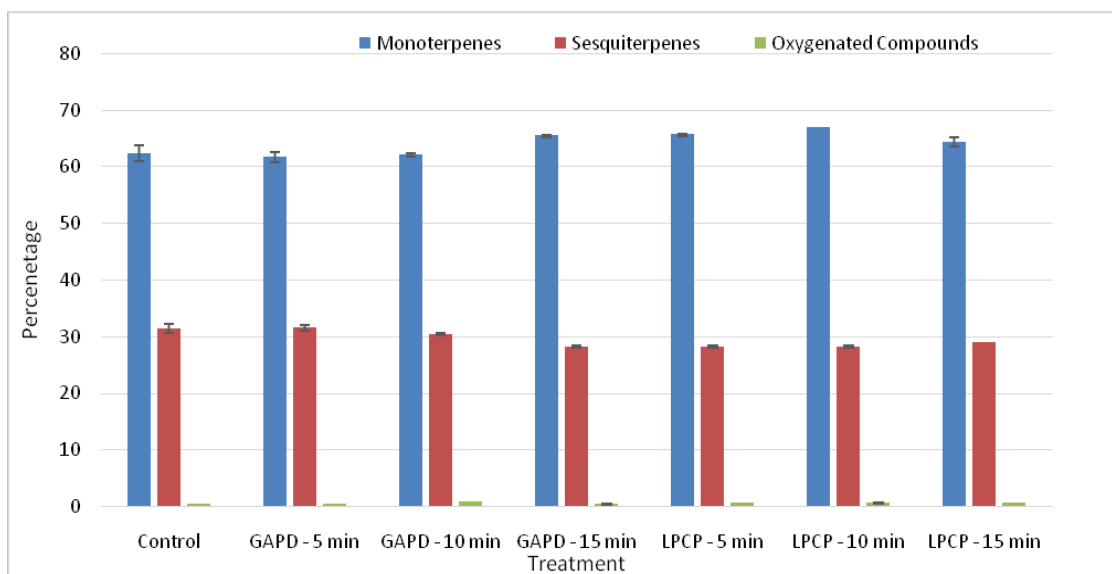


Figure 2: Variation of volatile oil components in GAPD and LPCP treatments

The term “top-peppery-note” is commonly associated with the monoterpene group, while the “pepper odor” is attributed to sesquiterpenes. Furthermore, the “body” of the pepper aroma is often linked to oxygen containing sesquiterpenes (Schulz *et al.*, 2005). As per the results obtained from GC MS and GC FID, it was observed as a reduction of sesquiterpene content might have an effect on the odor of the black pepper seeds after GAPD treatment.

In LPCP treatment, there was no significant difference ($P > 0.05$) in monoterpenes content of the volatile oils, sesquiterpene content significantly ($P < 0.05$) decreased after 15 min treatment. Monoterpene content varied in between 62 – 67 % while sesquiterpenes ranged from 27 – 32 % by weight complying to the available literature even after exposing to the LPCP treatment. Sesquiterpenes content decreased from 31.00 to 28.22 % after 10 min treatment and however the amount again increased up to 29.02 % keeping the composition well within the typical ranges. These results further confirm that the 5-minute treated black pepper seeds are more with preserved quality than further treatment times confirming the suitability of 5-minute LPCP treatment as a pretreatment for hydro distillation process.

CONCLUSION

The study focused on the capability of Low-Pressure Cold Plasma (LPCP) and Gliding Arc Plasma Discharge (GAPD) treatment to be used as a pretreatment method for hydro-distillation. The ideal treatment times were 5 minutes and 10 minutes respectively for the LPCP and GAPD to extract maximum quantity of volatile oils. Results confirmed both LPCP and GAPD does not affect the quality of Volatile Oils extracted from black pepper seeds undesirably during the selected processing times revealing the applicability as a potential pretreatment technology. However, more scaled up research are required to confirm the process parameters prior to commercial level applications.

ACKNOWLEDGEMENT

The collaborative research initiative spanning from 2017 to 2019, titled “Indo Sri Lanka Joint Research Project (FP/125),” brought together the Industrial Technology Institute (ITI) under the State Ministry of Technology, Government of Sri Lanka, and the Institute of Chemical Technology (ICT) in Mumbai, operating under the Department of Science, Government of India.

REFERENCES

1. Adamovich, I., Agarwal, S., Ahedo, E., Alves, L. L., Baalrud, S., Babaeva, N., Bogaerts, A., Bourdon, A., Bruggeman, P. J., Canal, C., Choi, E. H., Coulombe, S., Donkó, Z., Graves, D. B., Hamaguchi, S., Hegemann, D., Hori, M., Kim, H. H., Kroesen, G. M. W., ... Von Woedtke, T. (2022). The 2022 Plasma Roadmap: low temperature plasma science and technology. *Journal of Physics D: Applied Physics*, 55(37). <https://doi.org/10.1088/1361-6463/ac5e1c>
2. Afshari, R., & Hosseini, H. (2014). Non-thermal plasma as a new food preservation method, Its present and future prospect. *Journal of Paramedical Sciences*, 5(1), 116–120. <https://doi.org/10.22037/jps.v5i1.5348>
3. Akishev, Y., Grushin, M., Karalnik, V., Kochetov, I., Napartovich, A., & Trushkin, N. (2010). Generation of atmospheric pressure non-thermal plasma by diffusive and constricted discharges in air and nitrogen at the rest and flow. *Journal of Physics: Conference Series*, 257(1). <https://doi.org/10.1088/1742-6596/257/1/012014>
4. Alashti, F. J., Sohbatzadeh, F., Ahmadian, S., Kenari, R. E., & Nazifi, E. (2024). Impact of atmospheric cold plasma pretreatment on morphology, structure, and chemical properties of clove (*Syzygium aromaticum*). *Lwt*, 191(December 2023). <https://doi.org/10.1016/j.lwt.2023.115639>
5. Annor, G. A., Marcone, M., Bertoft, E., & Seetharaman, K. (2014). Physical and molecular characterization of millet starches. *Cereal Chemistry*, 91(3), 286–292. <https://doi.org/10.1094/CCHEM-08-13-0155-R>
6. Ansari, A., Parmar, K., & Shah, M. (2022). A comprehensive study on decontamination of food-borne microorganisms by cold plasma. *Food Chemistry: Molecular Sciences*, 4(February), 100098. <https://doi.org/10.1016/j.fochms.2022.100098>
7. Bußler, S. (n.d.). Cold atmospheric pressure plasma treatment of food matrices: Tailored modification of product properties along value-added chains of plant and animal related products (Issue September 2016).
8. Can Başer, K. H., & Buchbauer, G. (2015). Handbook of essential oils: Science, technology, and applications, second edition. In *Handbook of Essential Oils: Science, Technology, and Applications, Second Edition*. <https://doi.org/10.1201/b19393>
9. Cherif, M. M., Assadi, I., Khezami, L., Ben Hamadi, N., Assadi, A. A., & Elfalleh, W. (2023). Review on Recent Applications of Cold Plasma for Safe and Sustainable Food Production: Principles, Implementation, and Application Limits. *Applied Sciences (Switzerland)*, 13(4). <https://doi.org/10.3390/app13042381>
10. Chiappim, W., de Paula Bernardes, V., Almeida, N. A., Pereira, V. L., Bragotto, A. P. A., Cerqueira, M. B. R., Furlong, E. B., Pessoa, R., & Rocha, L. O. (2023). Effect of Gliding Arc Plasma Jet on the Mycobiota and Deoxynivalenol Levels in Naturally Contaminated Barley Grains. *International Journal of Environmental Research and Public Health*, 20(6). <https://doi.org/10.3390/ijerph20065072>
11. Chizoba Ekezie, F. G., Sun, D. W., & Cheng, J. H. (2017). A review on recent advances in cold plasma technology for the food industry: Current applications and future trends. *Trends in Food Science and Technology*, 69, 46–58. <https://doi.org/10.1016/j.tifs.2017.08.007>
12. Do, D. N. (2022). Hydrodistillation of Essential Oil from the Whole Black Pepper and Light Berries Black Pepper (*Piper Nigrum* L.) Harvesting in Dak Nong, Vietnam on a Pilot Scale: The Study on Extraction Process and Analyses of Essential Components. *AIP Conference Proceedings*,

- 2610(August). <https://doi.org/10.1063/5.0099580>
13. Ebadi, M. (2019). Effect of cold plasma on essential oil content and composition of lemon verbena. October 2018, 1166–1171. <https://doi.org/10.1002/fsn3.876>
 14. Fitzpatrick, J. J., van Lauwe, A., Coursol, M., O'Brien, A., Fitzpatrick, K. L., Ji, J., & Miao, S. (2016). Investigation of the rehydration behaviour of food powders by comparing the behaviour of twelve powders with different properties. *Powder Technology*, 297, 340–348. <https://doi.org/10.1016/j.powtec.2016.04.036>
 15. Hertwig, C., Meneses, N., & Mathys, A. (2018). Cold atmospheric pressure plasma and low energy electron beam as alternative nonthermal decontamination technologies for dry food surfaces: A review. *Trends in Food Science and Technology*, 77(October 2017), 131–142. <https://doi.org/10.1016/j.tifs.2018.05.011>
 16. Heydari, M., Carbone, K., Gervasi, F., Parandi, E., Rouhi, M., Rostami, O., Abedi-Firoozjah, R., Kolaoudou-Nasiri, A., Garavand, F., & Mohammadi, R. (2023). Cold Plasma-Assisted Extraction of Phytochemicals: A Review. In *Foods* (Vol. 12, Issue 17). <https://doi.org/10.3390/foods12173181>
 17. Jansz, E. R., Balachandran, S., Packiyasoathy, E. V., & Ratnayake, S. (1984). Effect of Maturity on some Chemical Constituents of Sri Lankan Pepper (*Piper nigrum* L.). 41–46.
 18. Kodama, S., Thawatchaipracha, B., & Sekiguchi, H. (n.d.). Enhancement of Essential Oil Extraction for Steam Distillation by DBD Surface Treatment. 126–132. <https://doi.org/10.1002/ppap.201300047>
 19. Kogelschatz, U. (2003). Dielectric-barrier discharges: Their History, Discharge Physics, and Industrial Applications. *Plasma Chemistry and Plasma Processing*, 23(1), 1–46. <https://doi.org/10.1023/A:1022470901385>
 20. Kuzminova, A., Kretková, T., Kylián, O., Hanuš, J., Khalakhan, I., Prukner, V., Doležalová, E., Šimek, M., & Biederman, H. (2017). Etching of polymers, proteins and bacterial spores by atmospheric pressure DBD plasma in air. *Journal of Physics D: Applied Physics*, 50(13). <https://doi.org/10.1088/1361-6463/aa5c21>
 21. Lee, H. S., Park, H. H., & Min, S. C. (2020). Microbial decontamination of red pepper powder using pulsed light plasma. *Journal of Food Engineering*, 284(March), 110075. <https://doi.org/10.1016/j.jfoodeng.2020.110075>
 22. Lee, Y. H., & Yeom, G. Y. (2005). Characteristics of a pin-to-plate dielectric barrier discharge in helium. *Journal of the Korean Physical Society*, 47(1), 74–78.
 23. Loureiro, A. da C., Souza, F. das C. d. A., Sanches, E. A., Bezerra, J. de A., Lamarão, C. V., Rodrigues, S., Fernandes, F. A. N., & Campelo, P. H. (2021). Cold plasma technique as a pretreatment for drying fruits: Evaluation of the excitation frequency on drying process and bioactive compounds. *Food Research International*, 147(May). <https://doi.org/10.1016/j.foodres.2021.110462>
 24. Misra, N. N., Pankaj, S. K., Segat, A., & Ishikawa, K. (2016). Cold plasma interactions with enzymes in foods and model systems. *Trends in Food Science and Technology*, 55, 39–47. <https://doi.org/10.1016/j.tifs.2016.07.001>
 25. Misra, N. N., Tiwari, B. K., Raghavarao, K. S. M. S., & Cullen, P. J. (2011). Nonthermal Plasma Inactivation of Food-Borne Pathogens. *Food Engineering Reviews*, 3(3–4), 159–170. <https://doi.org/10.1007/s12393-011-9041-9>
 26. Pepper, B., Piper, F., Dosoky, N. S., Satyal, P., Barata, L. M., Kelly, J., Silva, R., & Setzer, W. N. (2019). Volatiles of Black Pepper Fruits (*Piper nigrum* L.). 1–13.
 27. Primc, G. (2022). Generation of Neutral Chemically Reactive Species in Low-Pressure Plasma.

- Frontiers in Physics, 10(May), 1–8. <https://doi.org/10.3389/fphy.2022.895264>
28. Sarangapani, C., Devi, Y., Thirundas, R., Annapure, U. S., & Deshmukh, R. R. (2015). Effect of low-pressure plasma on physico-chemical properties of parboiled rice. *LWT - Food Science and Technology*, 63(1), 452–460. <https://doi.org/10.1016/j.lwt.2015.03.026>
 29. Sarangapani, C., Thirumdas, R., Devi, Y., Trimukhe, A., Deshmukh, R. R., & Annapure, U. S. (2016). Effect of low-pressure plasma on physico-chemical and functional properties of parboiled rice flour. In *Lwt* (Vol. 69). Elsevier Ltd. <https://doi.org/10.1016/j.lwt.2016.02.003>
 30. Schulz, H., Baranska, M., Quilitzsch, R., Schütze, W., & Lösing, G. (2005). Characterization of peppercorn, pepper oil, and pepper oleoresin by vibrational spectroscopy methods. *Journal of Agricultural and Food Chemistry*, 53(9), 3358–3363. <https://doi.org/10.1021/jf048137m>
 31. Setiawan, Y., Prayitnoadi, R. P., & Saputra, E. (2019). Essential oil processing of pepper process with aluminium condenser. *IOP Conference Series: Earth and Environmental Science*, 353(1). <https://doi.org/10.1088/1755-1315/353/1/012060>
 32. Shishir, M. R. I., Karim, N., Bao, T., Gowd, V., Ding, T., Sun, C., & Chen, W. (2020). Cold plasma pretreatment—A novel approach to improve the hot air drying characteristics, kinetic parameters, and nutritional attributes of shiitake mushroom. *Drying Technology*, 38(16), 2134–2150. <https://doi.org/10.1080/07373937.2019.1683860>
 33. Shishpanov, A. I., Bazhin, P. S., Ivanov, D. O., & Meschanov, A. V. (2020). Low-frequency one-electrode discharge in long tubes at low gas pressure. *Plasma Research Express*, 2(1). <https://doi.org/10.1088/2516-1067/ab7e83>
 34. Submitted, A. T., The, F. O. R., Of, D., & Engineering, D. O. F. (2011). Characterization , Comparison and Application of Two Types of Atmospheric Pressure Cold Argon Plasma Jets DOCTOR OF ENGINEERING DEPARTMENT OF PRODUCTION SCIENCE AND GRADUATE SCHOOL OF ENGINEERING.
 35. Tabibian, S. A., Labbafi, M., Askari, G. H., Rezaeinezhad, A. R., & Ghomi, H. (2020). Effect of gliding arc discharge plasma pretreatment on drying kinetic , energy consumption and physico-chemical properties of saffron (*Crocus sativus* L .). *Journal of Food Engineering*, 270(June 2019), 109766. <https://doi.org/10.1016/j.jfoodeng.2019.109766>
 36. Thirumdas, R., Kadam, D., & Annapure, U. S. (2017a). Cold Plasma : an Alternative Technology for the Starch Modification. *Food Biophysics*. <https://doi.org/10.1007/s11483-017-9468-5>
 37. Thirumdas, R., Kadam, D., & Annapure, U. S. (2017b). Cold Plasma: an Alternative Technology for the Starch Modification. *Food Biophysics*, 12(1), 129–139. <https://doi.org/10.1007/s11483-017-9468-5>
 38. Valencia, A., Laurindo, B., Laroque, D. A., Tiemi, S., Augusto, B., & Carciofi, M. (2022). Cold plasma in food processing: Design , mechanisms , and application. 312(April 2021). <https://doi.org/10.1016/j.jfoodeng.2021.110748>
 39. Yang, X., Cheng, J. H., & Sun, D. W. (2024). Enhancing microorganism inactivation performance through optimization of plate-to-plate dielectric barrier discharge cold plasma reactors. *Food Control*, 157(July 2023), 110164. <https://doi.org/10.1016/j.foodcont.2023.110164>
 40. Yu, H., Zhang, Y., Wong, A., De Rosa, I. M., Chueh, H. S., Grigoriev, M., Williams, T. S., Hsu, T., & Hicks, R. F. (2014). Atmospheric and Vacuum Plasma Treatments of Polymer Surfaces for Enhanced Adhesion in Microelectronics Packaging. *Adhesion in Microelectronics*, 9781118831, 137–172. <https://doi.org/10.1002/9781118831373.ch4>
 41. Ziuzina, D. (2015). ARROW @ TU Dublin Atmospheric Cold Plasma as a Tool for Microbiological Control. 0–258. <https://doi.org/10.21427/D7FW2Z>

**Photocatalytic degradation of methylene blue dye using silver nanoparticles prepared from
*Raphanus sativus***

M Y F Hasna¹, S Anuluxan¹, S Prabagar², R C L De Silva², S Thuraisingam³, J Prabagar^{*1}

¹Department of Chemistry, University of Jaffna, Sri Lanka.

²Industrial Technology Institute, Colombo, Sri Lanka.

³Palmyrah Research Institute, Sri Lanka

ABSTRACT

Green synthesis of silver nanoparticles possesses many merits compared to that of chemical synthetic methods. Silver nanoparticles have been widely used in many applications such as catalytic activity, dye degradation, antimicrobial and anti-inflammatory activities. In this study silver nanoparticles (AgNps) were synthesized using extract of *Raphanus sativus* roots and identified by the UV-Visible spectrophotometer. XRD peaks of the crystal confirmed the face-centered cubic silver crystals with size of 49.16 nm. FT-IR spectrum indicated the functional groups on this nanoparticles. Scanning electron microscope images showed the spherical shapes and size of the AgNps. The photocatalytic degradation of methylene blue was performed by altering the weight of silver nanoparticles and moles of NaBH₄. The degradation mixtures of 5 mg AgNps and 5 mL of NaBH₄, 10 mg AgNps and 5 mL of NaBH₄ and 10 mg AgNps and 10 mL of NaBH₄ attain degradation of 5.088%, 83.86 % and 48.067% of the methylene blue respectively. This study revealed that green synthesized silver nanoparticles from the extract of *Raphanus sativus* can act as a photocatalytic dye degradation agent against methylene blue.

Key words: Green synthesis, AgNPs, XRD, dye degradation, methylene blue

INTRODUCTION

Environmental pollution is one of the major problems currently the world is facing. Among other pollutions, water pollution is an urgent crisis as flora and fauna depend on the water for their survival. Industries including textile and apparel use of large quantities of water for fabric processing and coloring. Organic dyes are being used for the coloring of textile products. Dye molecules consist of two components namely the chromophores and auxochromes. The chromophores are mainly responsible for production of color (Gupta, 2009). There are several dyes used in the industries such as basic, acidic, reactive, azo, mordant, vat, disperse and sulfur dyes (Demirbas et al., 2009). The major types of dyes used in the industries are also said to be azo derivative dyes (Forgacs et al., 2004).

Cationic, anionic and nonionic dyes are another way of classification among the dyes (Salleh et al., 2011). Methylene blue is classified under cationic dye and has been widely used in the apparel industry and acute exposure can lead to cyanosis, quadriplegia, necrosis and vomiting (Vadivelan et al., 2005). So, these dyes should be removed from the industrial effluents before it is released into the environment. Several methods have been used for the treatment of wastewater containing organic dyes namely incineration (Lee et al., 2001), biological treatment (García-Montaño et al., 2008), ozonation (Chu et al., 2000) and adsorption on solid phases (Prado et al., 2003). But these processes have the following drawbacks: the incineration can produce toxic byproducts, biological treatment takes a long time and bad odor and the ozonation have a short half-life and the stability of ozone is affected by the pH, temperature and presence of salts (Chekir et al., 2016). The heterogeneous photocatalysis becomes a suitable treatment for the organic dye degradation. Many catalysts have been widely used to degrade the dye molecules such as TiO_2 (Hadei et al., Khasawneh et al., 2021), ZnO (Ahmad et al., Nguyen et al., 2021), silver nanoparticles (Seerangaraj et al., Sharma et al., 2021), graphene (Wang et al., 2021), graphene oxide (Zhang et al., 2021) and reduced graphene oxide (Bibi et al., 2019).

Nanotechnology is the hot topic in science which is focusing on the synthesis of nano size materials and their applications across all field of science including synthetic and biological chemistry (Fakhari et al., 2019). Nanoparticles comprises of novel chemical, physical and biological properties due to their size and large surface with free dangling bonds which results in higher reactivity when compared to that of bulk materials (Sharma et al., 2020). Silver nanoparticles are being widely used in many applications such as antibacterial (Thi Lan Huong & Nguyen et al., 2021; Anuluxan et al., 2022), antifungal (Mallmann et al., 2015), anti-inflammatory (Jain et al., 2019), and photocatalytic activities (Chand et al., 2021) due to its merits such as ecofriendly, nonallergic, nonirritant and heat resistant nature as well as chemically stable nature (Miri et al., 2018).

Many synthetic methods are available to produce silver nanoparticles such as chemical reduction, light assisted methods, electrochemical methods, and green synthetic method (Pacioni et al., 2015). Green synthetic method is an environmentally friendly method that involves the plant material, fungi or bacteria for the reduction of silver ions to metallic silver. This method has been widely investigated because of its non-toxicity and the usage of low amount of chemicals. Many plant materials have been used form silver nanoparticles such as Turmeric (Alsammarrarie et al., 2018), *Turbinaria ornata* (Anuluxan et al., 2022), *Diospyros lotus* (Hamedi et al., 2019), *Berberis vulgaris* (Behravan et al., 2019), and *Lysiloma acapulcensis* (Garibo et al., 2020). Plant parts contain

primary and secondary metabolites which reduces and stabilizes the formed nano-particles (Irshad et al., 2021). The study reported that *Raphanus sativus* has consist of many biologically active compounds such as flavonoids, phenols, terpenes, glucosinolate and fatty acids (Gamba et al., 2021). Therefore, this research focused on the synthesis of silver nanoparticles using *Raphanus sativus* root and photocatalytic activity of prepared silver nanoparticles was evaluated by the methylene blue (MB) degradation exposed to light irradiation. The effect of experimental conditions, such as amount of catalyst and concentration of NaBH₄ were studied.

METHODOLOGY

Preparation of Silver nanoparticles

Roots of *Raphanus sativus* were washed in deionized water and then the skins were removed from the roots and cut into small pieces. It was shadow dried for 7 days and grounded into powder and stored at room temperature. 5 g of *Raphanus sativus* (Figure 1) powder was added to 100 mL of deionized water and heated at 70 °C for 20 minutes. Then the aqueous solution was filtered and filtrate was stored in a refrigerator at 4°C.



Figure 2: Dried root sample of *Raphanus sativus*

10 mL of aqueous extract was taken in a conical flask and covered with aluminum foil. Then the aqueous extract was added with 90 mL of 5 mM AgNO₃. Solution pH was maintained at 3, 5, 7, 9, and 11. Reaction mixtures were stirred in a shaker for 24 hours at 300 rpm (Fadel and Al-Mashhedy, 2017). It was stored at room temperature until further analysis.

Characterization of AgNps

The silver nanoparticles were characterized with the UV-Visible spectrophotometer (Jasco V-570 UV/VIS/NIR) with 200 nm to 800 nm scanning range. The phase purity and the crystallinity of silver nanoparticles were analyzed by powder X-ray diffraction (XRD) (PANalytical-AERIS). The XRD pattern was obtained with Cu K α radiation ($\lambda=1.5408 \text{ \AA}$) at room temperature, with the operational conditions of accelerated voltage 40 kV and emission current of 44mA. The crystalline size of the nanoparticles was calculated using Scherrer equation,

$$D = \frac{K\lambda}{\beta \cos\theta} \quad (1)$$

Where K – Scherrer constant, λ – X-ray wavelength, β – the line broadening at half the maximum intensity, θ – Bragg's angle and D – crystalline size. M Y F Hasna et al., JSLAAS, Vol. 6, Issue 1 (2024) 39-49 by Hitachi SU6600 FE-SEM (Field Emission Scanning Electron Microscope) using carbon tapes.

Evaluation of photo catalytic degradation of methylene blue

Green synthesized 5 mg of AgNps and 5 mL of 1mM NaBH₄ were added into 50 mL methylene blue solution (10 ppm). A control was prepared in a similar manner without addition of AgNps. The mixtures were stirred under dark condition for 30 minutes to attain equilibrium. Then the mixtures were kept under light irradiation with stirring until its complete decolorized and the samples were withdrawn at 30 minutes interval and analyzed with UV-Vis spectrophotometer (Arunachalam et al., 2012). The following parameters were chosen to obtain the optimum condition for the photocatalytic degradation; 5 mg of AgNps and 5 mL of 1 mM NaBH₄ (a), 10 mg of AgNps and 5mL of 1mM NaBH₄ (b), and 10 mg of AgNps and 10mL of 1mM NaBH₄ (c). The degradation percentage was calculated by the following equation.

$$R = \frac{(C_0 - C_t)}{C_0} \times 100\%$$

RESULTS AND DISCUSSION

Characterization of silver nano-particles

The colour change from yellow to dark brown were observed after the incubation period from the shaker which is due to the reduction of Ag⁺ ion to Ag metallic nanoparticles. The production of nanoparticles was checked at various pH using UV-Visible spectrophotometer. As shown in the figure 2, UV-Visible peak at 430 nm confirmed the AgNps formation and the highest intensity peak was observed at pH 9 and the lowest peak was observed at pH 7. The formation of peaks around the 430 nm are due to surface plasmon resonance effect which is caused by the excitation of the electrons and passed to the conduction band of nanoparticles (Gul et al, 2016). The figure 3 shows that the colour became intense with the increase of pH

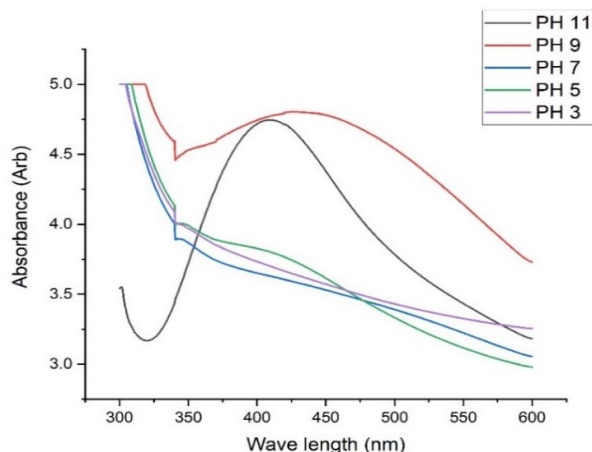


Figure 3: UV-Visible spectrum of synthesized AgNps at different pH

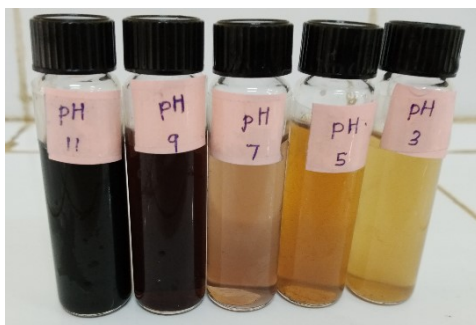


Figure 4: Colour of the AgNps mixture after 24 hours of incubation period

The crystalline nature of the synthesized AgNps was analyzed using X-ray crystallography. Figure 4 clearly shows the pattern of synthesized AgNps and main peaks of 38.32° , 44.59° , 64.91° , 78.16° and 82.44° corresponds to the planes of (111), (200), (220), (311), and (222) respectively. These planes confirmed the face-centered cubic silver crystals. The nanoparticle size was found to be 49.16 nm which indicate green synthesized AgNps falls under nanoparticle range.

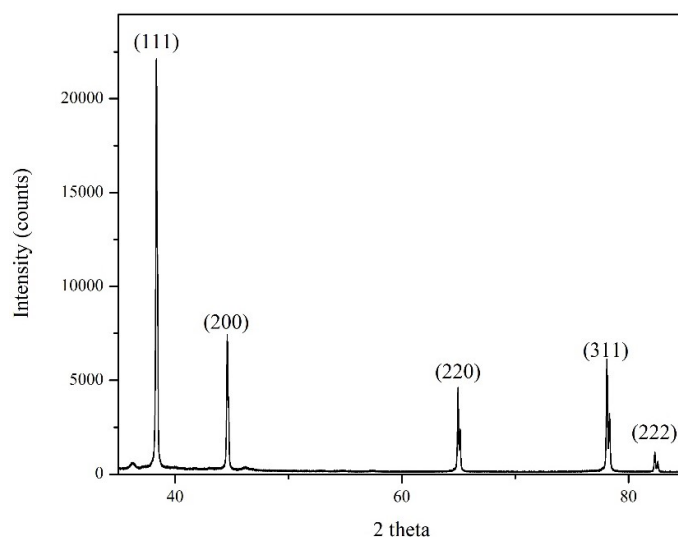


Figure 5: XRD Spectrum of synthesized AgNps

FT-IR spectroscopic technique contributes significantly in the identification of the functional groups which are present in the plant extract. The functional groups are responsible for the reduction of silver ions from silver nitrate and stabilized the synthesized AgNps. FT-IR spectrum of the synthesized AgNps is shown in Figure 5. The absorption peak at 1347cm^{-1} was assigned to the C-H bending frequency of alkane and 1037cm^{-1} is due to the C-C stretching frequency of alkane. The peak at 1590cm^{-1} was arisen due to the bending frequency of N-H bond of primary amines and the peak at 3280cm^{-1} corresponds to the stretching frequency of the O-H bond of hydroxyl groups. Protein molecules could be present in the plant extract and act as a stabilizing and reducing agent. Gole *et al.* (2001) mentioned that the cysteine from the protein molecules can bind to the AgNps and prevent aggregation by functioning as the capping or stabilizing agent. Gamba, *etal* (2021) reported that the sprout of *Raphanus sativus* contains glucosinolates, flavonoids, β -carotene.

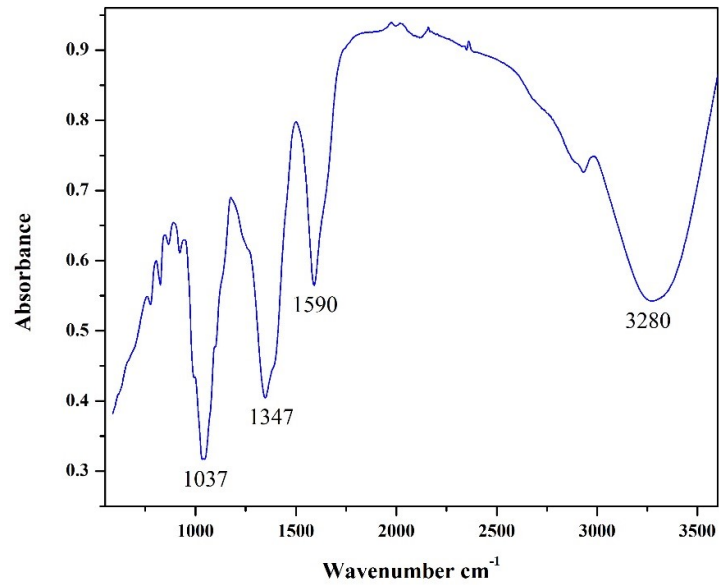


Figure 6: FT-IR spectrum of AgNps

SEM images show the surface morphology of the AgNps and most of the synthesized nanoparticles were found in spherical shapes (Figure 6). SEM images of the nanoparticles revealed that the nanoparticles were found in size below 100 nm.

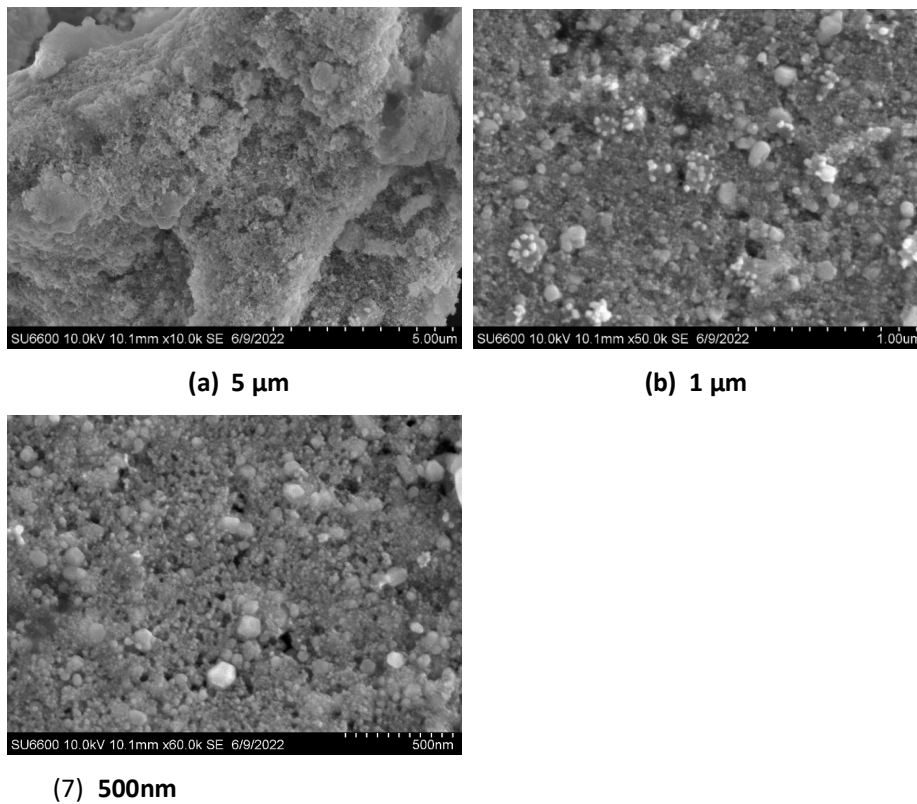


Figure 7: SEM images of synthesized AgNPs

Photo catalytic degradation of methylene blue

Figure 7 a-c shows the photo catalytic degradation of methylene blue where the parameters such as weight of AgNps and NaBH₄ were altered. Maximum absorbance of MB was observed in UV/Visible spectrometer at 670 nm. The effect of initial concentration of AgNps under light source was studied by using two different concentrations of the initial AgNps (5 and 10 mg per 50 mL) with 10 mgL⁻¹ concentration of MB dye as shown in Figures 7a and 7b. The rate of degradation was found to be 5.088 % at 240 minutes with 5 mg AgNps and 5 mL of NaBH₄ and with 10 mg AgNps and 5 mL of NaBH₄ attained 83.86 % at 45 minutes. When concentration of AgNps was increased from 5 to 10 mg, the photo catalytic activity was found to be increasing, this is due to the higher number of active sites on the catalyst. But the degradation rate decreased with NaBH₄ concentration (Figures 7c). The rate of degradation was found to be 48.067 % at 45 minutes with 10 mg AgNps and 10 mL of NaBH₄. The results indicate that 10 mg AgNps and 5 mL of NaBH₄ are the most active concentration in the degradation of methylene blue dye.

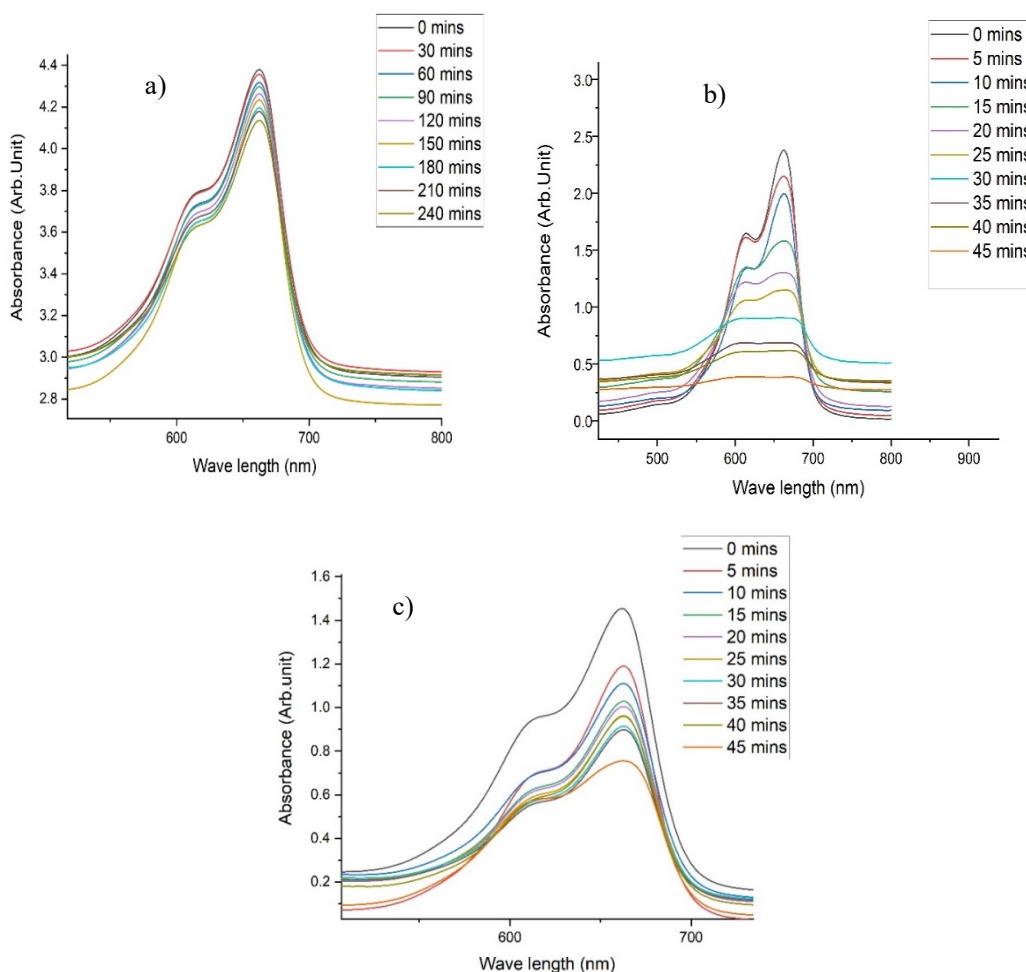


Figure 8: UV Vis spectrum of (a) 5 mg AgNps + 5 mL NaBH₄) (b) 10 mg AgNps + 5 mL NaBH₄) (c) 10 mg AgNps + 10 mL NaBH₄)

The rate of photocatalytic degradation of MB was shown in the plot of $\ln(C/C_0)$ versus time, t at different experiments a, b and c, (Figures 8a-c).

$$\ln \frac{C}{C_0} = -kt \tag{2}$$

where, C_0 is the initial concentrations of MB in solution and C is the concentration at times t , and k is the first-order rate constant. The kinetics study (Figure 8 a-c) reveals that the MB degradation belongs to first-order kinetics and the rate constants are 2.26536×10^{-4} , 0.03912 and 0.00923 for degradation mixtures a, b and c while correlation constants R^2 , for the fitted lines were 0.97973 , 0.97065 , and 0.91637 respectively.

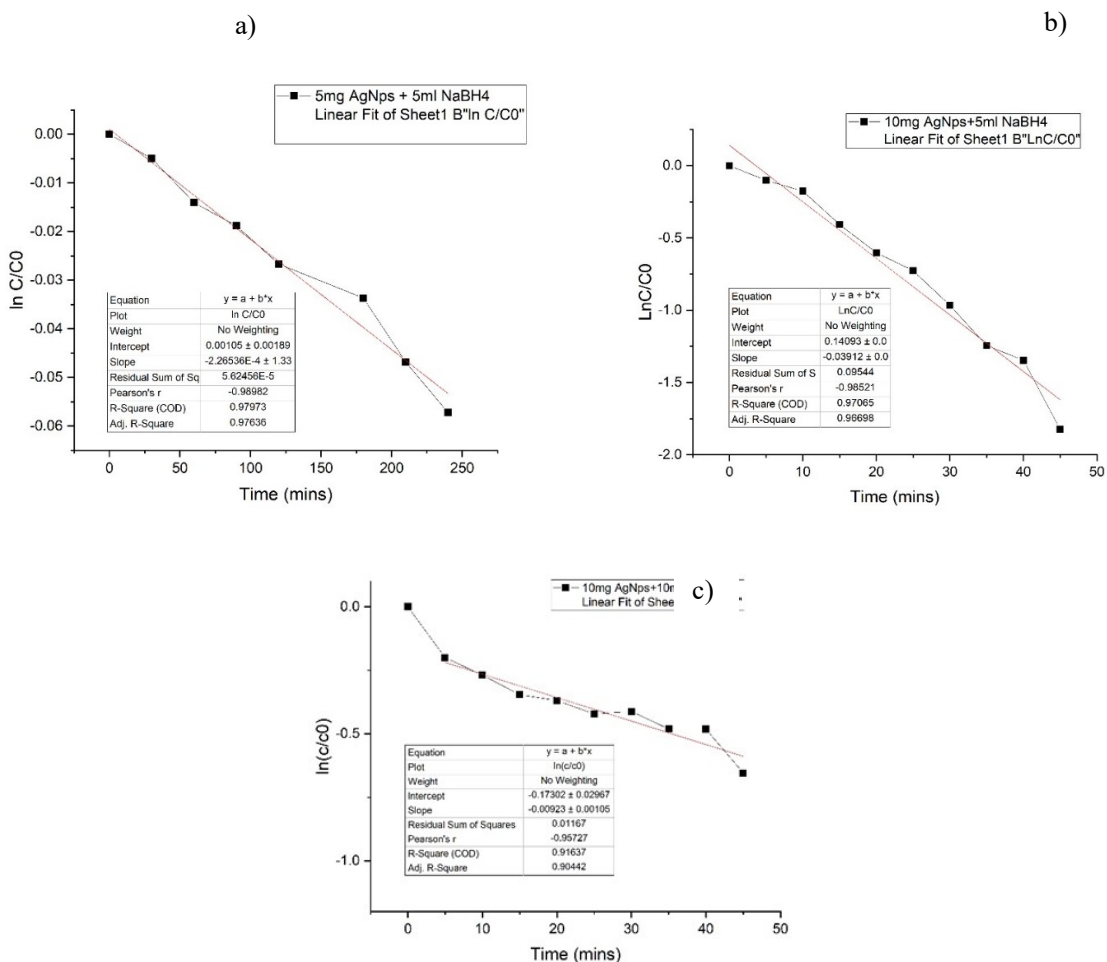


Figure 9: Kinetic study of photocatalytic degradation of methylene blue a) 5 mg Ag, 5 mL NaBH₄, b) 10 mg Ag, 5 mL NaBH₄, c) 10 mg Ag, 10 mL NaBH₄

CONCLUSION

Silver nanoparticles have been successfully synthesized from the aqueous extract of the *Raphanus sativus* root sample and their performance toward the degradation of hazardous organic dyes was studied. The UV-Visible peak found at 430 nm shows the formation of AgNps. XRD pattern of the

AgNps reveals that the green synthesized AgNps were the face-centered cubic silver crystals. The crystallite size of the synthesized nanoparticles was 49.16 nm. FT-IR spectram confirms the presence of functional groups such as primary amines, free hydroxyl alcohol and phenol which can be due to the presence of protein molecules in the plant extract of *Raphanus sativus*. The degradation of MB dye was performed and a higher percentage of degradation was achieved with mixtures of 10 mg AgNps and 5 mL of NaBH₄. Biosynthesized AgNps can be effectively utilized to degrade various environmentally hazardous organic dyes.

ACKNOWLEDGMENTS

The authors thank the Royal Norwegian Embassy in Sri Lanka for the donation of XRD under capacity building and establishment of research consortium project (Number LKA – 3182 – HRNCET) and AHEAD, ELTA-ELSE Development Project, Department of Chemistry, University of Jaffna for the provision of SEM spectra of the AgNps.

FUNDING

This research did not receive any specific grant from funding agencies.

REFERENCES

1. Ahmad, M.; Rehman, W.; Khan, M. M.; Qureshi, M. T.; Gul, A.; Haq, S.; Ullah, R.; Rab, A.; Mena, F. J. J. o. E. C. E., Phytogenic fabrication of ZnO and gold decorated ZnO nanoparticles for photocatalytic degradation of Rhodamine B. *Journal of Environmental Chemical Engineering* **2021**, *9* (1), 104725.
2. Alsammarraie, F. K.; Wang, W.; Zhou, P.; Mustapha, A.; Lin, M. J. C.; Biointerfaces, S. B., Green synthesis of silver nanoparticles using turmeric extracts and investigation of their antibacterial activities. *Colloids and Surfaces B: Biointerfaces* **2018**, *171*, 398-405.
3. Anuluxan, S.; Thavaranjit, A.; Prabagar, S.; De Silva, R.; Prabagar, J. J. C. P., Synthesis of silver nanoparticles from *Turbinaria ornata* and its antibacterial activity against water contaminating bacteria. *Chemical Papers* **2022**, *76* (4), 2365-2374.
4. Arunachalam, R.; Dhanasingh, S.; Kalimuthu, B.; Uthirappan, M.; Rose, C.; Mandal, A. B., Phytosynthesis of silver nanoparticles using *Coccinia grandis* leaf extract and its application in the photocatalytic degradation. *Colloids and surfaces. B, Biointerfaces* **2012**, *94*, 226-30.
5. Behravan, M.; Panahi, A. H.; Naghizadeh, A.; Ziaee, M.; Mahdavi, R.; Mirzapour, A. J. I. j. o. b. m., Facile green synthesis of silver nanoparticles using *Berberis vulgaris* leaf and root aqueous extract and its antibacterial activity. *International journal of biological macromolecules* **2019**, *124*, 148-154.
6. Bibi, S.; Ahmad, A.; Anjum, M. A. R.; Haleem, A.; Siddiq, M.; Shah, S. S.; Al Kahtani, A. J. J. o. E. C. E., Photocatalytic degradation of malachite green and methylene blue over reduced graphene oxide (rGO) based metal oxides (rGO-Fe₃O₄/TiO₂) nanocomposite under UV-visible light irradiation. *Journal of Environmental Chemical Engineering* **2021**, *9* (4), 105580.
7. Chand, K.; Jiao, C.; Lakhan, M. N.; Shah, A. H.; Kumar, V.; Fouad, D. E.; Chandio, M. B.; Maitlo, A. A.; Ahmed, M.; Cao, D. J. C. P. L., Green synthesis, characterization and photocatalytic activity of silver nanoparticles synthesized with *Nigella Sativa* seed extract. *Chemical Physics Letters* **2021**, *763*, 138218
8. Chekir, N.; Benhabiles, O.; Tassalit, D.; Laoufi, N. A.; Bentahar, F. J. D.; Treatment, W., Photocatalytic degradation of methylene blue in aqueous suspensions using TiO₂ and ZnO. *Desalination and Water Treatment* **2016**, *57* (13), 6141-6147.

9. Chu, W.; Ma, C.-W. J. W. r., Quantitative prediction of direct and indirect dye ozonation kinetics. *Water research* **2000**, *34* (12), 3153-3160.
10. Demirbas, A., Agricultural based activated carbons for the removal of dyes from aqueous solutions: a review. *Journal of hazardous materials* **2009**, *167* (1-3), 1-9.
11. Fakhari, S.; Jamzad, M.; Fard, H., Green synthesis of zinc oxide nanoparticles: a comparison. *Green Chemistry Letters and Reviews* **2019**, *12*, 19-24.
12. Fadel, Q.; Al-Mashhedy, L. J. B. I. J., Biosynthesis of silver nanoparticles using peel extract of *Raphanus sativus* L. *Biotechnol Ind J* **2017**, *13* (1), 120.
13. Forgacs, E.; Cserhádi, T.; Oros, G., Removal of synthetic dyes from wastewaters: a review. *Environment International* **2004**, *30* (7), 953-971.
14. Gamba, M.; Asllanaj, E.; Raguindin, P. F.; Glisic, M.; Franco, O. H.; Minder, B.; Bussler, W.; Metzger, B.; Kern, H.; Muka, T. J. T. i. F. S.; Technology, Nutritional and phytochemical characterization of radish (*Raphanus sativus*): A systematic review. *Trends in Food Science & Technology* **2021**, *113*, 205-218.
15. García-Montaña, J.; Domènech, X.; García-Hortal, J. A.; Torrades, F.; Peral, J. J. J. o. h. m., The testing of several biological and chemical coupled treatments for Cibacron Red FN-R azo dye removal. *Journal of hazardous materials* **2008**, *154* (1-3), 484-490.
16. Garibo, D.; Borbón-Nuñez, H. A.; de León, J. N. D.; García Mendoza, E.; Estrada, I.; Toledano-Magaña, Y.; Tiznado, H.; Ovalle-Marroquin, M.; Soto-Ramos, A. G.; Blanco, A. J. S. r., Green synthesis of silver nanoparticles using *Lysiloma acapulcensis* exhibit high-antimicrobial activity. *Scientific reports* **2020**, *10* (1), 1-11.
17. Gole, A.; Dash, C.; Ramakrishnan, V.; Sainkar, S.; Mandale, A.; Rao, M.; Sastry, M. J. L., Pepsin-gold colloid conjugates: preparation, characterization, and enzymatic activity. *Langmuir* **2001**, *17* (5), 1674-1679
18. Gul, S.; Ismail, M.; Khan, M. I.; Khan, S. B.; Asiri, A. M.; Rahman, I. U.; Khan, M. A.; Kamboh, M. A. J. A. P. J. o. T. D., Novel synthesis of silver nanoparticles using melon aqueous extract and evaluation of their feeding deterrent activity against housefly *Musca domestica*. *Asian Pacific Journal of Tropical Disease* **2016**, *6* (4), 311-316.
19. Gupta, V. J. J. o. e. m., Application of low-cost adsorbents for dye removal—a review. *Journal of Environmental Management* **2009**, *90* (8), 2313-2342.
20. Hadei, M.; Mesdaghinia, A.; Nabizadeh, R.; Mahvi, A. H.; Rabbani, S.; Naddafi, K. J. E. S.; Research, P., A comprehensive systematic review of photocatalytic degradation of pesticides using nano TiO₂. *Environmental Science and Pollution Research* **2021**, *28* (11), 13055-13071.
21. Hamedi, S.; Shojaosadati, S. A. J. P., Rapid and green synthesis of silver nanoparticles using *Diospyros lotus* extract: Evaluation of their biological and catalytic activities. *Polyhedron* **2019**, *171*, 172-180.
22. Irshad, M. A.; Nawaz, R.; Rehman, M. Z. u.; Adrees, M.; Rizwan, M.; Ali, S.; Ahmad, S.; Tasleem, S., Synthesis, characterization and advanced sustainable applications of titanium dioxide nanoparticles: A review. *Ecotoxicology and Environmental Safety* **2021**, *212*, 111978.
23. Jain, A.; Anitha, R.; Rajeshkumar, S. J. R. J. o. P.; Technology, Anti-inflammatory activity of Silver nanoparticles synthesized using Cumin oil. *Research Journal of Pharmacy and Technology* **2019**, *12* (6), 2790-2793.
24. Khasawneh, O. F. S.; Palaniandy, P. J. E. T.; Innovation, Removal of organic pollutants from water by Fe₂O₃/TiO₂ based photocatalytic degradation: A review. *Environmental Technology & Innovation* **2021**, *21*, 101230.

25. Lee, J.-K.; Gu, J.-H.; Kim, M.-R.; Chun, H.-S. J. J. o. c. e. o. J., Incineration characteristics of dye sludge in a fluidized bed incinerator. *Journal of chemical engineering of Japan***2001**,*34* (2), 171-175.
26. Mallmann, E. J. J.; Cunha, F. A.; Castro, B. N.; Maciel, A. M.; Menezes, E. A.; Fechine, P. B. A. J. R. d. I. d. M. T. d. S. P., Antifungal activity of silver nanoparticles obtained by green synthesis. *Revista do Instituto de Medicina Tropical de São Paulo***2015**,*57*, 165-167.
27. Miri, A.; Shahraki Vahed, H. O.; Sarani, M. J. R. o. C. I., Biosynthesis of silver nanoparticles and their role in photocatalytic degradation of methylene blue dye. *Research on Chemical Intermediates***2018**,*44* (11), 6907-6915.
28. Nguyen, D. T. C.; Le, H. T.; Nguyen, T. T.; Nguyen, T. T. T.; Bach, L. G.; Nguyen, T. D.; Van Tran, T. J. J. o. H. M., Multifunctional ZnO nanoparticles bio-fabricated from *Canna indica* L. flowers for seed germination, adsorption, and photocatalytic degradation of organic dyes. *Journal of Hazardous Materials***2021**,*420*, 126586.
29. Pacioni, N. L.; Borsarelli, C. D.; Rey, V.; Veglia, A. V., Synthetic routes for the preparation of silver nanoparticles. In *Silver nanoparticle applications*, Springer: 2015; pp 13-46.
30. Prado, A. G.; Miranda, B. S.; Jacintho, G. V. J. S. S., Interaction of indigo carmine dye with silica modified with humic acids at solid/liquid interface. *Surface Science***2003**,*542* (3), 276-282.
31. Salleh, M. A. M.; Mahmoud, D. K.; Karim, W. A. W. A.; Idris, A., Cationic and anionic dye adsorption by agricultural solid wastes: A comprehensive review. *Desalination* **2011**,*280* (1), 1-13.
32. Seerangaraj, V.; Sathiyavimal, S.; Shankar, S. N.; Nandagopal, J. G. T.; Balashanmugam, P.; Al-Misned, F. A.; Shanmugavel, M.; Senthilkumar, P.; Pugazhendhi, A. J. J. o. E. C. E., Cytotoxic effects of silver nanoparticles on *Ruellia tuberosa*: Photocatalytic degradation properties against crystal violet and coomassie brilliant blue. *Journal of Environmental Chemical Engineering***2021**,*9* (2), 105088.
33. Sharma, R. J. M. T. P., Synthesis of *Terminalia bellirica* fruit extract mediated silver nanoparticles and application in photocatalytic degradation of wastewater from textile industries. *Materials Today: Proceedings* **2021**,*44*, 1995-1998.
34. Sharma, R.; Sarkar, A.; Jha, R.; Kumar Sharma, A.; Sharma, D., Sol-gel-mediated synthesis of TiO₂ nanocrystals: Structural, optical, and electrochemical properties. *International Journal of Applied Ceramic Technology* **2020**,*17* (3), 1400-1409.
35. Thi Lan Huong, V.; Nguyen, N. T., Green synthesis, characterization and antibacterial activity of silver nanoparticles using *Sapindus mukorossi* fruit pericarp extract. *Materials Today: Proceedings* **2021**,*42*, 88-93.
36. Vadivelan, V.; Kumar, K. V., Equilibrium, kinetics, mechanism, and process design for the sorption of methylene blue onto rice husk. *Journal of colloid and interface science* **2005**,*286* (1), 90-100.
37. Wang, Y.; Qiang, Z.; Zhu, W.; Yao, W.; Tang, S.; Yang, Z.; Wang, J.; Duan, J.; Ma, C.; Tan, R. J. A. A. N. M., BiPO₄ nanorod/graphene composite heterojunctions for photocatalytic degradation of tetracycline hydrochloride. *ACS Applied Nano Materials***2021**,*4* (9), 8680-8689.
38. Zhang, R.; Ma, Y.; Lan, W.; Sameen, D. E.; Ahmed, S.; Dai, J.; Qin, W.; Li, S.; Liu, Y. J. U. s., Enhanced photocatalytic degradation of organic dyes by ultrasonic-assisted electrospray TiO₂/graphene oxide on polyacrylonitrile/β-cyclodextrin nanofibrous membranes. *Ultrasonics sonochemistry***2021**,*70*, 105343.

I. GENERAL INSTRUCTIONS

1) Research presented in the manuscript could be in any field of science. 2) The research work should not have been published or submitted for publication elsewhere. 3) A corresponding author who will be responsible for all communications with the SLAAS Office should be identified. 4) Submission of manuscripts: Manuscripts can be submitted online <https://journal.slaas.lk/>. 5) Certificate of authenticity: Declaration form should be duly filled, signed by all authors and attach separately. 6) Submissions that involve human or animal trials should provide evidence of approval obtained by an ethics review committee.

II. SPECIFIC INSTRUCTIONS TO AUTHORS

1. Document to be submitted: Manuscript in MS Word format.

2. Format for typesetting

- Paper size: A4 (210 x 297) typed single sided only.
- Margins: Top, bottom and right margins of 25 mm and a left margin of 30 mm.
- Line spacing: 1.5
- Length: Length of the manuscript including text, tables, figures and references should not exceed 15 typed pages.
- Page and line numbering: All pages should be sequentially numbered using Arabic Numbers.
- Font: Arial font, size 12. Language/spelling: UK English only.
- Software: Authors may use either MS Word for Windows or the Macintosh equivalent.

3 Names and affiliations

- Title and running title (less than 25 Characters). They should be in bold faced letters
- Name/s and affiliation/s of author/s
- Email address, mailing address and contact numbers of the corresponding author. Note: Identified the corresponding author by placing an asterisk after the name.

(At the first submission only the manuscript without the names of authors and affiliations to be uploaded with the filled declaration form)

4. Abstract

- Should be limited to a maximum of 250 words.
- Up to a maximum of the five (05) key word should be identified, arranged in alphabetical order, included immediately after the abstract.
- Abstract should be typed in italics. Scientific names in the abstract should be underlined.
- No reference, tables, or figures should be included in the abstract.

5. Body

- Introduction: Justification of the research work, objectives and hypotheses should be included in the introduction.
- Methods and Materials/ Methodology: All materials, chemicals, clinical, subjects and samples used should be identified. Analytical, survey and statistical method should be explained concisely. Common analytical methods need not be elaborated.
- Results and Discussion: Can be combined.
- Conclusions: Should be concise.
- Headings: All headings should be in bold capital and centered, e.g., INTRODUCTION
- Subheadings: All subheadings should be in bold and in title case, e.g., Preparation of Land.
- Non-English terms: All non-English terms should be italicized, e.g., et al., i.e., viz., except "etc."
- References: Use APA style 3

6. Table and Figures

- Should be included in the exact place within the text
- Tables should be numbered sequentially using Arabic numerals. The titles should be self explanatory and placed above the tables.
- Tabled should not contain any vertical lines
- Illustration, Line drawing and photographs, if any, should be clear, properly numbered and captioned and ready for reproduction. They should be of high and resolution such as minimum of 300 dpi and saved in .tif or .bmp formats. Please do not use .jpeg or similar formats that do not reproduce well.

- All lettering, graph lines and points on graphs should be sufficiently large and bold faced to permit reproduction for inclusion in the Journal.
- Artworks and illustrations should be of appropriate thickness. Please note that thin lines do not reproduce well. Please note that the illustrations, line drawings and photographs should be placed in the appropriate location of the electronic file and numbered sequence with other figures.

7. Units

- SI units should be used.
- A single space should be left between the numerical value and the unit.

8. Acronyms and Abbreviations

- All acronyms should be written in full at the first time of appearance. Abbreviations can be used subsequently.
- The full stop should not be included in abbreviations. Where abbreviations are likely to cause ambiguity or may not be readily understood by readers, the units should be mentioned in full.

9. On being informed of the acceptance, the manuscripts should be revised as per the reviewers' suggestions and re-submitted to the Editor – SLAAS. The accepted manuscripts will be published in the inaugural Journal of the SLAAS. Manuscripts that do not confirm to the above guidelines will not be accepted.

10. Acknowledgements Only the essential individuals and/or organizations/institutes should be include 11. Need to attach the manuscripts both as 1. with names and affiliations of the author and 2. Without with names and affiliations of the author

*Journal of the Sri Lanka Association for
the Advancement of Science*

Volume 6 Issue 1

Research Articles

Effect of CT Simulator Tube Voltages on CT Number and Relative Electron Density of CT Images
P De Sliva, A H Dilip Kumara, K L Priyalal, K L I Gunawardhana

Incorporation of Wood ash and waste glass powder in enhancing concrete block performance
V T Prarthana, R C L De Silva, P Subramanium, S Thuraisingam, J Prabagar

*Low-Pressure and Atmospheric-Pressure Cold Plasma Treatment as a Pretreatment for Extracting Volatile Oils from Black Pepper
(Piper nigrum) Seeds*
B G C J De Silva, H D Weerathunge, P N R J Amunugoda, S H P Gunawrdena, A A P de Alwis

Photocatalytic degradation of methylene blue dye using silver nanoparticles prepared from Raphanus sativus
M Y F Hasna, S Anuluxan, S Prabagar, R C L De Silva, S Thuraisingam, J Prabagar



9771391025002

Edited and Published by the Sri Lanka Association of for the Advancement of Science

e-ISSN 2682-6992